Journal of Materials Processing Tech. 318 (2023) 118037

Contents lists available at ScienceDirect

Journal of Materials Processing Tech.

journal homepage: www.elsevier.com/locate/jmatprotec

A new analytical model for force prediction in incremental sheet forming

Hui Zhu, Hengan Ou *

Department of Mechanical, Materials and Manufacturing Engineering, Faculty of Engineering, University of Nottingham, Nottingham NG7 2RD, UK

ARTICLE INFO

Associate Editor: Marion Merklein

Keywords:
Incremental sheet forming
Force prediction
Analytical method
Deformation behaviour
Contact condition

ABSTRACT

A new analytical model for forming force prediction in the whole process of incremental sheet forming (ISF) is presented in this work. The modelling of contact region, thickness distribution and strain components are carried out as the basis for the prediction of vertical and horizontal forces. The effect of local contact behaviour and material deformation, as well as the behaviours of global bending, changes of deformation mode and contact condition are taken into account in the modelling of ISF force history. The force prediction model at both plane strain and biaxial tension condition areas is developed based on the differences in contact region and thickness distribution between these two different deformation states. Validated by ISF tests for a truncated cone and pyramid part with varying drawing angles, the prediction of force history captures well the fluctuation of different force components due to the change of deformation conditions and provides an insight into the material deformation mechanisms and the direct correlation to forming force characteristics of the whole ISF process. In a practical case, the model is successfully applied to the force prediction in ISF-based cranial plate manufacture. The model is also validated by a series of ISF tests with accurate force predictions of both the peak and stabilised forces.

1. Introduction

As an emerging flexible manufacturing process, incremental sheet forming (ISF) has drawn increasing attention in recent years (Duflou et al., 2017). Extensive research has shown that it is especially advantageous in manufacturing small-batch and customised sheet parts because of its distinctive features of flexibility (Bowen et al., 2022), adaptability (Schafer and Schraft, 2005), applicability (Emmens et al., 2010), improved material formability (Nirala and Agrawal, 2022) and associated benefits in energy efficiency and reduced costs (Cooper and Gutowski, 2020). Great potential has been shown in practical applications of ISF in aerospace, automotive industries, and medical engineering. Chang and Chen (2022) developed a novel flexible free ISF without edge constraint and tested the possibility to manufacture skull implant, turbo tip and blade. Centeno et al. (2012), adapted ISF in the application of hole flanging, while Takano et al. (2008) tested the feasibility of cold recycling of sheet metal waste by ISF.

In ISF processing, the designed shape is achieved by local deformation in steps, which is driven by often a hemispheric forming tool following a contour path (Zhu et al., 2020) on usually a computer numerical control (CNC) milling machine (Kopac and Kampus, 2005), a designed ISF machine (Allwood et al., 2005) or a robotic manufacturing system (Mohanty et al., 2019). The contact between the forming tool and the sheet material is important to the deformation, formability and fracture in ISF (Jackson and Allwood, 2009). The forming forces in ISF also reflect the tool-sheet contact relationship due to friction (Lu et al., 2014), bending, shearing and stretching effect (Li et al., 2015), tool rotation (Obikawa et al., 2009), and the steadiness of contact (Ren et al., 2018).

The forming force in ISF is influenced by process parameters including step size, forming tool dimension, drawing angle, sheet thickness, feed rate, spindle speed, temperature, lubricant condition and material property (Kumar et al., 2019). Filice et al. (2006) observed the trend of force variation in ISF and clarified that the initial bending leads to the peak force. After peak, the stretching begins and there are three distinguished trends: steady-state, polynomial and monotonically decreasing trends. Duflou et al. (2007a) presented a sudden change when the tool starts to enter each contour or deforms corner positions of a pyramid part although there was no significant difference of the mean total forces in ISF of cones and pyramids. These indicate the effect of initial bending and geometric shape on the force variations in ISF.

Accurate prediction of forming force provides an insight into the material deformation and the interaction between ISF parameters and it is feasible to even detect fracture failure (Ambrogio et al., 2006). To predict the forming forces in the whole process of ISF, finite element

* Corresponding author.
E-mail addresses: huizhucn@outlook.com (H. Zhu), h.ou@nottingham.ac.uk (H. Ou).

https://doi.org/10.1016/j.jmatprotec.2023.118037
Received 11 March 2023; Received in revised form 13 May 2023; Accepted 20 May 2023
Available online 22 May 2023

Nomenclature

Symbol (unit)	Description
r (mm)	Distance from studied position to tool centre
φ (rad)	Angle from studied position to tool axis
θ (rad)	Angle from workpiece meridional cross-section to studied position
x, y, z (mm)	Coordinates of tool position in x, y, and z axes
r_{tool} (mm)	Tool radius
t_0 (mm)	Initial sheet thickness
Δz (mm)	Step size
Ψ (rad)	Designed drawing angle
α (rad)	Actual drawing angle
α_b (rad)	Actual drawing angle at corner of pyramid part
β, λ (rad)	Indentation angle in workpiece meridional and circumferential directions
β_b (rad)	β angle at corner of pyramid part
μ (rad)	Elastic recovery angle
β_1 (rad)	Angle induced by forming tool increment in workpiece meridional direction
β_{1b} (rad)	β_1 angle at corner of pyramid part
t (mm)	Thickness of sheet material below forming tool at different regions
Δt (mm)	Sheet thickness reduction at different regions after contact
t_b (mm)	Thickness in workpiece meridional direction at corner of pyramid part
Δt_{er} (mm)	Maximum instant thickness recovery
t_c (mm)	Sheet thickness below tool centre
$\overline{\sigma}_c$ (MPa)	Mean equivalent stress of sheet material below tool centre
$\overline{\varepsilon}_c^p$	Mean equivalent plastic strain of sheet material below tool centre
w_{er} (mm)	Maximum width of elastic recovery region
t_A, t_B (mm)	Thicknesses of sheet material in Parts A and B
φ_p (rad)	φ angle of projection position on workpiece meridional cross-section
t_p (mm)	Thickness of projection position on workpiece meridional cross-section
ω (rad)	Arc angle from studied position to projection position on workpiece circumferential cross-section
ρ_d, ρ_{er} (mm)	Thickness reduction rates of deformation and elastic recovery regions
E (MPa)	Young's modulus of sheet material
n	Strain hardening exponent of sheet material
R_b, R_0, R (mm)	Distances from part centre/symmetry axis to edge of backing plate, initial tool position and studied tool position
r_{gb} (mm)	Global bending radius
h (mm)	Depth of tool position
$\varepsilon_{stretching}$	Stretching strain of the neutral surface
$\varepsilon_{bending}$	Bending strain of sheet material
ε_φ, ε_θ, ε_r	Strain in tool meridional, circumferential and radial directions
$\overline{\sigma}$ (MPa)	Equivalent stress of sheet material
$\overline{\varepsilon}^p$	Equivalent plastic strain of sheet material
F, F_v, F_h, F_r, F_t (N)	Total, vertical, horizontal, radial, and tangential forces
F_{ls} (N)	Localised shear force
P1, P2	Boundaries of overlapping deformation region in plane strain condition
P3	Boundary of non-overlapping deformation region in plane strain condition
P4, P5	Boundaries of elastic recovery region in plane strain condition
a_{P1}, a_{P2}, a_{P4}, a_{P5} (mm)	Semi-major axes of ellipses for P1, P2, P4 and P5
b_{P1}, b_{P2}, b_{P4}, b_{P5} (mm)	Semi-minor axes of ellipses for P1, P2, P4 and P5
F_{ls}^{P1}, F_{ls}^{P2}, F_{ls}^{P3}, F_{ls}^{P4}, F_{ls}^{P5} (N)	Localised shear forces of P1–P5
Q1	Boundary of corner deformation region in biaxial tension condition
Q2	Boundary of overlapping deformation region in biaxial tension condition
Q3, Q4	Boundaries of elastic recovery region in biaxial tension condition
a_{Q1}, a_{Q2}, a_{Q3}, a_{Q4} (mm)	Semi-major axes of super ellipse or ellipses for Q1–Q4
b_{Q1}, b_{Q2}, b_{Q3}, b_{Q4} (mm)	Semi-minor axes of super ellipse or ellipses for Q1–Q4
F_{ls}^{Q1}, F_{ls}^{Q2}, F_{ls}^{Q3}, F_{ls}^{Q4} (N)	Localised shear forces of Q1–Q4
F_v^{ls} (N)	Vertical component of localised shear force
F_v^{gb} (N)	Vertical force from global bending
F_t^{ls} (N)	Tangential component of localised shear force
F_t^{mt} (N)	Tangential force leading to material thinning
F_t^f (N)	Frictional force in tangential direction
F_x, F_y (N)	Forces along x and y axes
f	Frictional coefficient between forming tool and sheet
σ_s (MPa)	Yield stress of sheet material at different regions
ε_s	Yield strain of sheet material at different regions
τ (MPa)	Shear stress of sheet material
γ (mm)	Elastic deflection
D (N·mm)	Flexural rigidity of sheet material
ν	Poisson's ratio of sheet material
$\overline{\varepsilon}_{gb}$	Equivalent strain due to global bending
$r_{gb}^{critical}$ (mm)	Critical bending radius for maximum elastic deflection
$h_{critical}$ (mm)	Critical depth of tool position for maximum elastic deflection

(FE) simulation is commonly used. However, a satisfactory FE simulation is affected by multiple factors and often takes considerable time to complete (Moser et al., 2021). Apart from FE simulation, machine learning has drawn increasing attention in force prediction of ISF (Ostasevicius et al., 2021). However, a machine learning dataset is necessarily generated from a series of tests (Najm and Paniti, 2023) or FE simulations (Jiang et al., 2022), which may take quite much time and effort. Therefore, it is highly desirable to develop analytical models for time and tool path dependent force prediction with sufficient accuracy and efficiency. In recent years, analytical methods have been used and validated in geometric accuracy improvement (Praveen et al., 2020), thickness distribution (Cao et al., 2015), surface roughness (Chang and Chen, 2019), and temperature distribution (Wu et al., 2020).

To predict ISF forming force, analytical models could be developed using experimental or theoretical based methods. The experimental based model requires a large number of testing results to establish the relationship equation between forming force and process parameters. Aerens et al. (2010) and Duflou et al. (2007b) attempted to predict ISF forces by analysing testing results under different parameters and fitting the regression equations with power functions. As a function of sheet thickness, drawing angle, tool diameter, step size and material tensile strength, Aerens et al. model was capable to predict three force components for five different sheet materials in the studied forming conditions.

On the other hand, theoretical based models could be developed by looking into the intrinsic relationships among ISF parameters, material

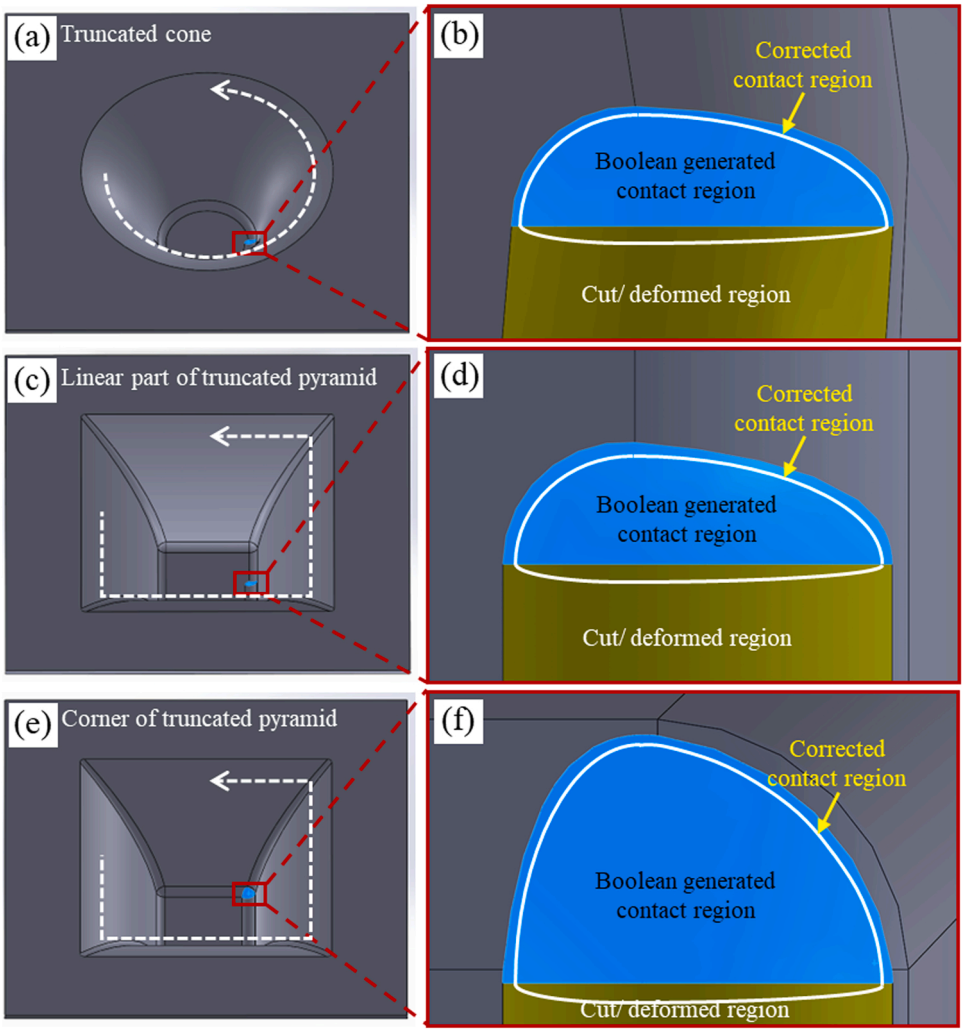

Fig. 1. Boolean subtraction of a ball tool from (a), (b) truncated cone shape, (c), (d) linear part and (e), (f) corner of truncated pyramid shape.

deformation, stress and strain states. Li et al. (2015) developed models based on the energy method, and took the deformation modes of shear, bending and stretching into account. The prediction results showed good agreement with experimental data, but Li et al. model requires further adjustment for a wider range of process conditions because this model only considers the prediction of horizontal force components and uses an empirical coefficient for combined shear and bending deformation. Bansal et al. (2017) presented equations for axial, radial and tangential forces, and the prediction of axial force was validated by comparing with experimental results although the modelling assumed a rectangle contact region and uniform stress distribution. Liu et al. (2022) developed an analytical model for force prediction in three directions by considering the contact area. The forming force in different directions is calculated by integrating the directional force of each element, which is the multiplication of the element area and the corresponding stress. However, several key parameters in the model are unknown and need to be determined by experimental results. Adopted from the membrane analysis by Silva et al. (2008), Chang et al. (2019) developed an analytical model to predict forming force in ISF and adjusted the model for several variants. This model calculates the forming force and components by multiplying the through-thickness stress on neutral surface with contact area and projection areas. For different ISF conditions, the prediction accuracy of the model was validated. However, without considering the force caused by global bending of unsupported sidewall, Chang et al. model can only be used to predict stabilised force instead of giving whole-process force prediction from the beginning to the end of ISF process.

As summarised from the above literature review, two of the existing but unsolved essential issues in analytical force prediction are the dramatically increased forming force by the deformation/contact behaviour change and the peak force by the initial bending effect. In order to overcome the limitations in existing analytical models, this work presents a novel modelling strategy for forming force history prediction by looking into the material deformation in ISF processes. Localised indentation, tool-sheet contact, material stretching, as well as previously less involved issues including global bending, deformation mode change and contact condition change are considered in ISF processing conditions. Experimental validations are conducted to test the prediction results of the analytical model as well as comparison with other representative models. The developed model could help to reveal and understand the complicated and instable deformation behaviour from both local and global aspects.

2. Analytical modelling of forming force

The modelling strategy and deviation process for forming force prediction are given in this section. The modelling of contact region, thickness distribution, strain and stress components is derived first followed by the calculation of forming force components.

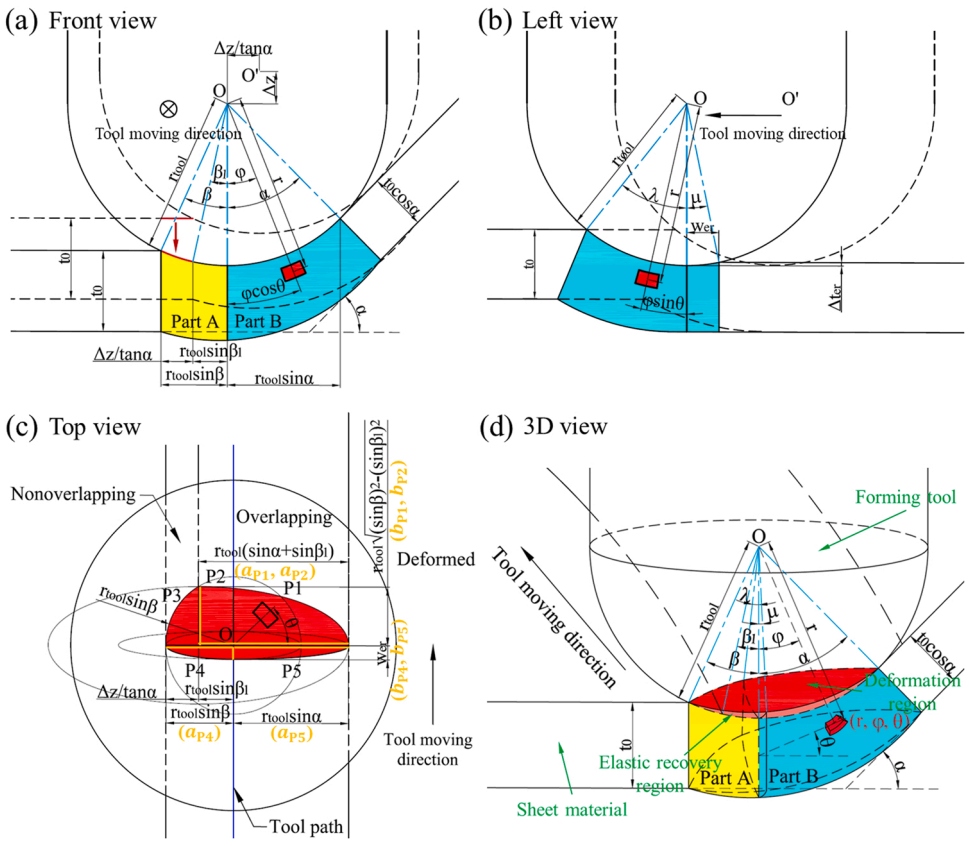

Fig. 2. Illustration of contact region in ISF and the coordinate system to show the relationship between forming tool and sheet material in plane strain condition from (a) front view, (b) left view, (c) top view and (d) 3D view.

2.1. Contact region

In ISF, larger contact area between forming tool and sheet material could contribute to larger forming force, while losing contact usually leads to smaller force. The first step of modelling is to identify the contact region.

The similarity between ISF and milling processes is that both obtain the final part through accumulation of localised deformation or cutting following a predefined tool path. The major difference is that the localised material under milling is subjected to cutting, while in ISF the localised sheet material undergoes plastic deformation followed by some elastic deformation. The ISF of rigid plastic materials may have the same contact region to the end milling process with a ball nose tool. As shown in Fig. 1, Boolean operation is used to subtract a ball tool from truncated cone and pyramid shaped parts. The blue area shows the cutting region in end milling process using a ball nose tool, which is the same as the contact region in ISF of materials only with rigid plastic deformation. However, the elastic deformation before full tool-sheet contact and the recovery after deformation should be considered in real ISF situation. A shrink of the front contact region and an expansion of the rear contact region may be applied, as shown by the white lines in Fig. 1. The above analysis is the basis for the modelling of contact region in ISF.

Before analytical modelling, a number of assumptions are made below:

(1) The scallop height is neglected as it is relatively small compared to the sheet thickness.
(2) The thickness of localised contact region is assumed linearly distributed in the workpiece meridional and circumferential directions.
(3) In the elastic recovery region, the maximum elastic recovery of thickness occurs at the sheet material below the tool centre position.

Under ISF condition, a localised spherical coordinate system is proposed with the origin at the tool centre. For a certain position or small element inside the contact region, the coordinate can be expressed as (r, φ,θ) as shown in Fig. 2, where r is the distance from the studied position to the tool centre, φ is the angle between the position and the tool axis, and θ is the angle from the workpiece meridional cross-section to the position. r_{tool} is the tool radius, t_0 is the initial sheet thickness, α is the drawing angle, β and λ are the indentation angles in the workpiece meridional and circumferential directions, respectively, μ is the elastic recovery angle behind the tool resulting from the instant recovery after elastoplastic deformation, and β_1 is the angle induced by the increment of forming tool in workpiece meridional direction. The partition of Parts A and B is for the convenience of thickness derivation on workpiece meridional cross-section, and Parts A and B are at inner and outer sides of the tool, respectively.

As indicated by Park and Kim (2003) and Martins et al. (2008), the normal state of ISF formed part is under plane strain condition. This is also revealed by the strain components distribution in FE simulation of ISF of 0.7 mm titanium grade 1 (TA1) sheet. As shown in Fig. 3(b) and (d), for the truncated cone part and the linear positions of truncated pyramid part, zero circumferential strain is observed along the dotted paths in Fig. 3(a) and (c). Therefore, plane strain condition can be regarded as the normal state after ISF at the level of global deformation.

In plane strain condition, the contact region may be comprised of three parts: non-overlapping deformation (ND), overlapping deformation (OD) and elastic recovery (ER) regions visible in a top view shown in Fig. 2(c), which can be seen as the combination of a part of a circular region and parts of three elliptical regions. The ND region covers the

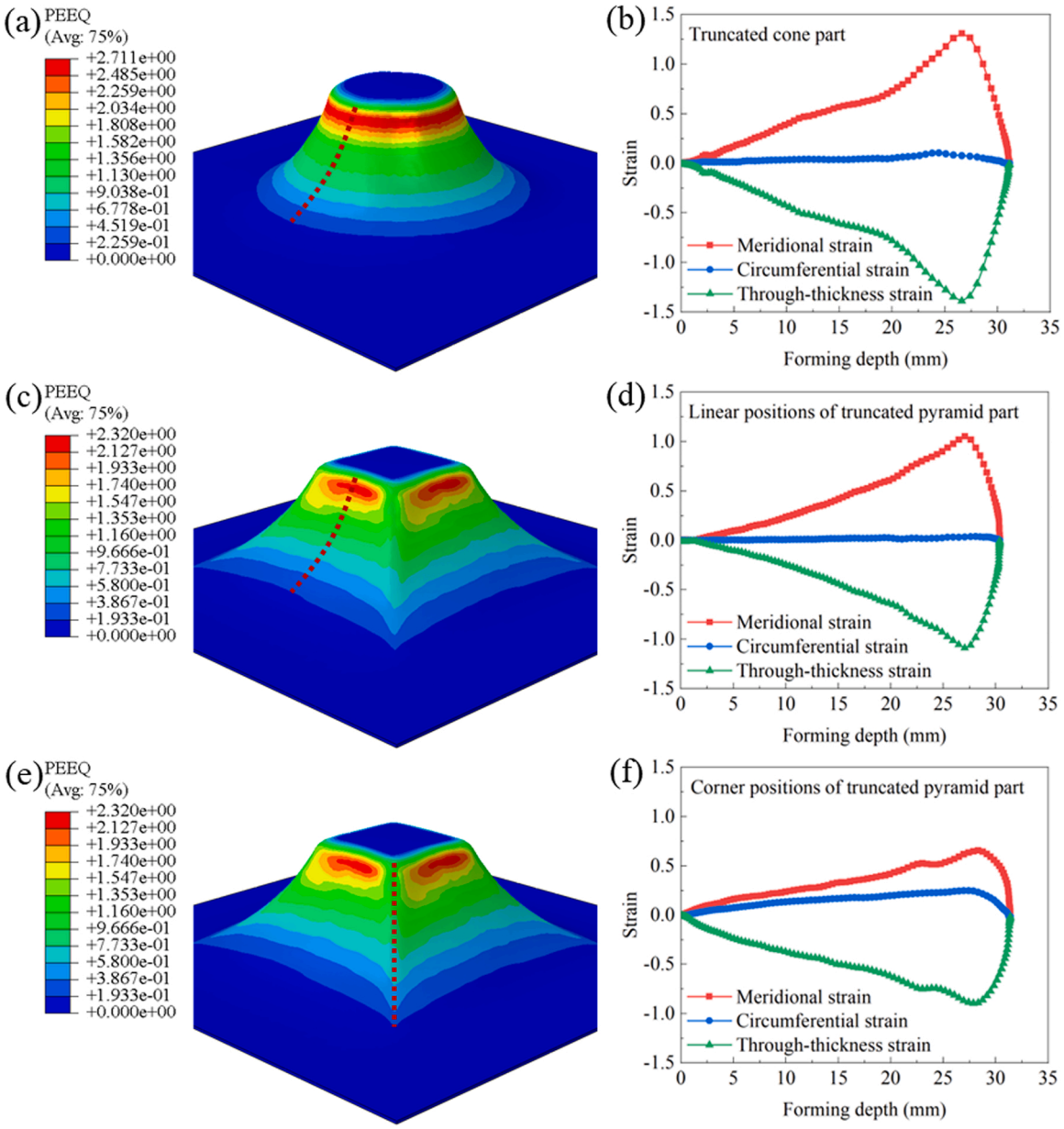

Fig. 3. FE simulation of TA1 ISF of (a) truncated cone part and (c), (e) truncated pyramid part, and (b), (d), (f) principal strain components distribution along the dotted path.

area where the sheet material is newly deformed under the tool, and P3 in Fig. 2(c) is the border line of this region. The OD region defines the material that has already undergone at least one deformation cycle before this round of tool contact, and the border line is composed of P1 and P2. ER region represents the area where the sheet material undergoes the instant elastic recovery after deformation, and Parts A and B of the ER region have the boundaries as P4 and P5, respectively, as given in Fig. 2(c). The definition of different regions is critical to the analytical modelling, as they are the key to derivation of the localised shear force, which may drive the material to move downwards.

For OD region, the ellipse (P1 and P2) in a horizontal projection plane has semi-major and semi-minor axes with lengths of $a_{P1} = a_{P2} = r_{tool} \bullet (\sin\alpha + \sin\beta_1)$ and $b_{P1} = b_{P2} = r_{tool} \bullet \sqrt{(\sin\beta)^2 - (\sin\beta_1)^2}$, respectively. By projecting the ellipse in the horizontal plane to the hemispherical tool surface, the centre is located at (r_{tool}, β_1, π), and the expression of the ellipse can be written as following:

$$\frac{(r_{tool} \bullet \sin\varphi \bullet \cos\theta + r_{tool} \bullet \sin\beta_1)^2}{{a_{P1}}^2} + \frac{(r_{tool} \bullet \sin\varphi \bullet \sin\theta)^2}{{b_{P1}}^2} = 1 \quad (1)$$

where β will be calculated in Section 2.3, and the relationship between β and β_1 can be given as following:

If the step size $\Delta z \le r_{tool} \bullet \sin\beta \bullet \tan\alpha$,

$$\beta_1 = \arcsin\left(\sin\beta - \frac{\Delta z}{r_{tool} \bullet \tan\alpha}\right) \quad (2)$$

and if $\Delta z \ge r_{tool} \bullet \sin\beta \bullet \tan\alpha$,

$$\beta_1 = \arcsin\left(\frac{\Delta z}{r_{tool} \bullet \tan\alpha} - \sin\beta\right) \quad (3)$$

The situation of $\Delta z \ge r_{tool} \bullet \sin\beta \bullet \tan\alpha$ leads to too small or even no overlapping region, which is uncommon in ISF design and would cause poor surface finish. Therefore, β_1 is calculated as Eq. (2) throughout the modelling.

For the circular shape of ND region (P3), the radius is $r_{tool} \bullet \sin\beta$. In the spherical coordinate system, the contact boundary of this region can be expressed as following:

$$\varphi = \beta \tag{4}$$

Parts A and B of ER region also have elliptical shapes (P4 and P5) with the tool tip as the centre, and $a_{P4} = r_{tool} \bullet \sin\beta$ and $a_{P5} = r_{tool} \bullet \sin\alpha$ as the length of semi-major axes, respectively. The length of semi-minor axis can be calculated with consideration of the elastic recovery of the sheet thickness after deformation. According to the assumption, the maximum elastic recovery of the sheet thickness occurs below the tool centre position, and the maximum recovery Δt_{er} may be calculated with the following equation by considering the elastic strain recovery:

$$\Delta t_{er} = \left[\exp\left(\frac{1}{2} \bullet \frac{\overline{\sigma}_c}{E}\right) - 1\right] \bullet \Delta t_c \tag{5}$$

where E is the Young's modulus, $\Delta t_c = t_0 - t_c$ is the thickness reduction below the tool centre position, and $\overline{\sigma}_c$ is the mean equivalent stress of the sheet material below the tool centre position. The calculation methods for t_c and $\overline{\sigma}_c$ are given in Sections 2.2 and 2.4, respectively.

The maximum width of the ER region w_{er}, i.e., the length of semi-minor axes b_{P4} and b_{P5} as shown in Fig. 2(c), is given as the following expression:

$$b_{P4} = b_{P5} = w_{er} = \sqrt{r_{tool}^2 - (r_{tool} - \Delta t_{er})^2} \tag{6}$$

As a result, in the spherical coordinate system, the boundaries of Parts A and B of ER region are expressed as the following Eqs. (7) and (8), respectively:

$$\frac{(r_{tool} \bullet \sin\varphi \bullet \cos\theta)^2}{a_{P4}^2} + \frac{(r_{tool} \bullet \sin\varphi \bullet \sin\theta)^2}{b_{P4}^2} = 1 \tag{7}$$

$$\frac{(r_{tool} \bullet \sin\varphi \bullet \cos\theta)^2}{a_{P5}^2} + \frac{(r_{tool} \bullet \sin\varphi \bullet \sin\theta)^2}{b_{P5}^2} = 1 \tag{8}$$

2.2. Thickness distribution under tool-sheet contact

This section aims to give the analytical model of sheet thickness distribution under tool-sheet contact. The modelling process is presented in two steps: thickness distribution on the workpiece meridional cross-section and thickness distribution of the whole contact region in 3D space.

The thickness distribution on the workpiece meridional cross-section is firstly derived. According to the assumption of linear thickness distribution, the thickness along the workpiece meridional direction as shown in Fig. 2(a) is linearly distributed from t_0 to $t_0 \bullet \cos\alpha$ following the cosine law (Hussain and Gao, 2007). So, the thickness t on the workpiece meridional cross-section at a proposed position with coordinates of (r_{tool}, φ,θ) (on the workpiece meridional cross-section, $\theta = 0$ in Part B or $\theta = \pi$ in Part A) can be expressed as the following equation:

$$t = t_0 - \frac{t_0 \bullet (1 - \cos\alpha) \bullet (\beta + \varphi \bullet \cos\theta)}{\alpha + \beta} \tag{9}$$

On the workpiece cross-section of Parts A and B, Eq. (9) can be written in the following formats, respectively:

$$t_A = t_0 - \frac{t_0 \bullet (1 - \cos\alpha) \bullet (\beta - \varphi)}{\alpha + \beta} \tag{10}$$

$$t_B = t_0 - \frac{t_0 \bullet (1 - \cos\alpha) \bullet (\beta + \varphi)}{\alpha + \beta} \tag{11}$$

The thickness at the tool centre position t_c can be calculated as following by applying $\varphi = 0$:

$$t_c = t_0 - \frac{t_0 \bullet (1 - \cos\alpha) \bullet \beta}{\alpha + \beta} \tag{12}$$

Thickness distribution of the whole contact region in 3D space can be obtained by following the derivation in Appendix A. The thickness distribution in ND and OD region is expressed as the following equation:

$$t = t_0 - \frac{t_0 \bullet (1 - \cos\alpha)}{\alpha + \beta} \bullet \left[\beta + \arcsin(\sin\varphi \bullet \cos\theta) - \frac{(\beta - \beta_1) \bullet \sqrt{1 - (\sin\beta_1)^2} \bullet \varphi \bullet \sin\theta}{\sqrt{\beta^2 - \beta_1^2} \bullet \sqrt{1 - (\sin\varphi \bullet \cos\theta)^2}}\right] \tag{13}$$

The thickness distribution in ER region is expressed as the following equation:

$$t = t_0 - \frac{t_0 \bullet (1 - \cos\alpha)}{\alpha + \beta} \bullet \left\{\beta + \arcsin(\sin\varphi \bullet \cos\theta) + \frac{\left[\exp\left(\frac{1}{2} \bullet \frac{\overline{\sigma}_c}{E}\right) - 1\right] \bullet \beta \bullet \varphi \bullet \sin\theta}{\arccos\left[1 - \left(\exp\left(\frac{1}{2} \bullet \frac{\overline{\sigma}_c}{E}\right) - 1\right) \bullet \frac{t_0 \bullet (1 - \cos\alpha) \bullet \beta}{r_{tool} \bullet (\alpha + \beta)}\right] \bullet \sqrt{1 - (\sin\varphi \bullet \cos\theta)^2}}\right\} \tag{14}$$

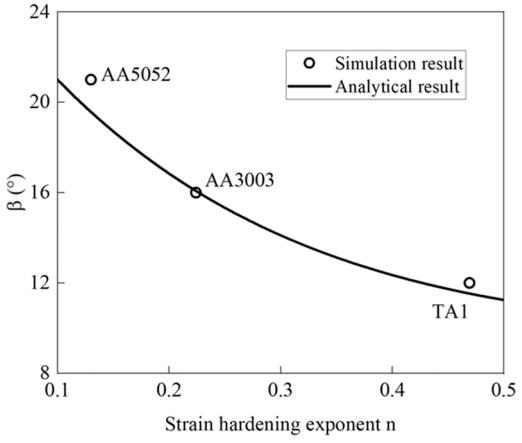

Fig. 4. Comparison of indentation angle between simulation and analytical results considering the effect of material hardening exponent on indentation in ISF process.

2.3. Indentation and drawing angles

In expressions of thickness distribution, Eqs. (13) and (14), there are two unknown parameters: equivalent stress $\overline{\sigma}_c$ at the tool centre position and the indentation angle β in workpiece meridional direction, among which $\overline{\sigma}_c$ can be calculated by using the equivalent plastic strain in the constitutive equation. Apart from β, the actual drawing angle α is different from the designed drawing angle Ψ because of the initial bending effect and the incomplete contact between the forming tool and sheet material. Therefore, the actual drawing angle α needs to be identified appropriately and affects the calculation of all the equations above. This section aims to give the detailed calculation methods of β and α.

As shown in Fig. 2(a), β meets the condition given by the following expression:

$$r_{tool} \bullet (1 - \cos\beta) > t_0 \bullet (1 - \cos\beta) \bullet \frac{\beta}{\alpha + \beta} \tag{15}$$

Referring to the study of Ai et al. (2017), strain hardening exponent n is considered in the modelling process to reflect the effect of material

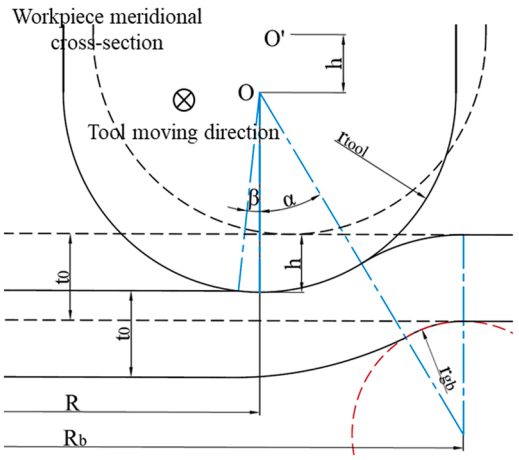

Fig. 5. Illustration of tool-sheet relationship to show the global bending effect at the beginning of ISF.

hardening on indentation, and an equation is proposed as following by modifying the above expression:

$$r_{\text{tool}} \bullet (1-\cos\beta) = t_0 \bullet (1-\cos\alpha) \bullet \frac{\beta}{\alpha+\beta} + \frac{1}{1+\exp(5 \bullet n-1)} \bullet r_{\text{tool}} \bullet (1-\cos\beta) \tag{16}$$

Solving the above equation gives the expression of β:

$$\beta = \frac{1}{2} \bullet \left[\sqrt{\alpha^2 + \frac{8 \bullet t_0 \bullet (1-\cos\alpha) \bullet [1+\exp(5 \bullet n-1)]}{r_{\text{tool}} \bullet \exp(5 \bullet n-1)}} - \alpha \right] \tag{17}$$

To confirm the validity of Eq. (17), FE simulation is used to obtain angle β of materials with different strain hardening exponent as it is difficult to observe in experiment. AA5052, AA3003 and TA1 are used in ISF simulation with drawing angle of 50° and sheet thickness of 1.2 mm. As shown in Fig. 4, the comparison between the simulation and analytical results indicates that the proposed equation can predict angle β well.

Since the boundary expressions of different regions are derived in Eqs. (1), (4), (7) and (8), the indentation angle λ in workpiece circumferential direction and the elastic recovery angle μ as shown in Fig. 2(b) can be approximately calculated as the following equations:

$$\lambda = \sqrt{\beta^2 - {\beta_1}^2} \tag{18}$$

$$\mu = \arcsin\frac{w_{\text{er}}}{r_{\text{tool}}} \tag{19}$$

Another important angle in the contact region is the drawing angle. At the initial stage of ISF, the actual drawing angle α is smaller than the designed drawing angle Ψ because the tool and the sheet are not in complete contact and the bending effect is obvious at the beginning. Fig. 5 illustrates the contact relationship at the beginning of ISF, in which the initial bending effect is demonstrated.

According to the geometric feature, following equations can be listed:

$$(r_{\text{gb}} + t_0 + r_{\text{tool}}) \bullet \sin\alpha = R_{\text{b}} - R \tag{20}$$

$$(r_{\text{gb}} + t_0) \bullet \cos\alpha + h - r_{\text{tool}} \bullet (1-\cos\alpha) = r_{\text{gb}} + t_0 \tag{21}$$

where R_{b} is the distance from the part centre/symmetry axis to the edge of backing plate (or clamping position if without backing plate), R is the distance from the part centre/symmetry axis to the tool position, r_{gb} is the bending radius and h is the depth of tool position. By solving Eqs. (20) and (21), the actual drawing angle at the initial stage of ISF can be obtained as the following expression:

$$\alpha = 2 \bullet \tan^{-1}\left(\frac{h}{R_{\text{b}} - R}\right) \tag{22}$$

The actual drawing angle follows Eq. (22) until the designed value Ψ is reached.

2.4. Strain components

In ISF, the forming force is closely related to the amount of deformation, which is quantified by strain components. This section gives the modelling and calculation of strain components under tool-sheet contact.

The strain distribution of the tool meridional cross-section may be calculated under the combined effect of stretching and local bending (Fang et al., 2014). The strain caused by stretching and material thinning on the neutral surface can be calculated as following:

$$\varepsilon_{\text{stretching}} = \ln\frac{t+\Delta t}{t} \tag{23}$$

where t is the material thickness under contact, which is derived as Eqs. (13) and (14) for different contact regions. $\Delta t = t_0 \bullet (1-\cos\alpha) \bullet (\beta-\beta_1)/(\alpha+\beta)$ for overlapping regions, while $\Delta t = t_0 - t$ for non-overlapping regions. The strain due to pure bending has the following expression (Hu et al., 2002):

$$\varepsilon_{\text{bending}} = \ln\frac{r}{\sqrt{r_{\text{tool}} \bullet (r_{\text{tool}} + t)}} \tag{24}$$

Combining the stretching and bending strain, the strain along the tool meridional direction can be calculated:

$$\varepsilon_{\varphi} = \varepsilon_{\text{stretching}} + \varepsilon_{\text{bending}} = \ln\frac{(t+\Delta t) \bullet r}{t \bullet \sqrt{r_{\text{tool}} \bullet (r_{\text{tool}} + t)}} \tag{25}$$

Although the global deformation and final state of the ISF formed truncated cone part are in plane strain condition, the instant local deformation state under the localised contact can be seen similar as stretch forming of thin sheet, which is typically in biaxial tension condition (Hu et al., 2002). Therefore, ε_{θ} and ε_{r} in the tool meridional and radial directions may be given by the next equations:

$$\varepsilon_{\theta} = \ln\frac{(t+\Delta t) \bullet r}{t \bullet \sqrt{r_{\text{tool}} \bullet (r_{\text{tool}} + t)}} \tag{26}$$

$$\varepsilon_{\text{r}} = 2 \bullet \ln\frac{t \bullet \sqrt{r_{\text{tool}} \bullet (r_{\text{tool}} + t)}}{(t+\Delta t) \bullet r} \tag{27}$$

The equivalent plastic strain $\bar{\varepsilon}^{\text{p}}$ can be derived as the following expression:

$$\bar{\varepsilon}^{\text{p}} = \frac{\sqrt{2}}{3} \bullet \sqrt{(\varepsilon_{\text{r}} - \varepsilon_{\varphi})^2 + (\varepsilon_{\varphi} - \varepsilon_{\theta})^2 + (\varepsilon_{\theta} - \varepsilon_{\text{r}})^2} = 2 \bullet \left| \ln\frac{(t+\Delta t) \bullet r}{t \bullet \sqrt{r_{\text{tool}} \bullet (r_{\text{tool}} + t)}} \right| \tag{28}$$

The equivalent stress $\bar{\sigma}$ can be calculated with a given material constitutive model and the equivalent plastic strain. It is noteworthy that $\bar{\sigma}_{\text{c}}$ in Eq. (5) can be obtained at the mean equivalent plastic strain $\bar{\varepsilon}^{\text{p}}_{\text{c}}$, which may be calculated without consideration of bending strain:

$$\bar{\varepsilon}^{\text{p}}_{\text{c}} = 2 \bullet \ln\frac{t_{\text{c}} + \Delta t}{t_{\text{c}}} \tag{29}$$

where, $\Delta t = t_0 \bullet (1-\cos\alpha) \bullet (\beta-\beta_1)/(\alpha+\beta)$ and t_{c} is derived as Eq. (12).

2.5. Forming force

After the modelling of contact region, thickness distribution, strain and stress components in the above several sections, this section aims to

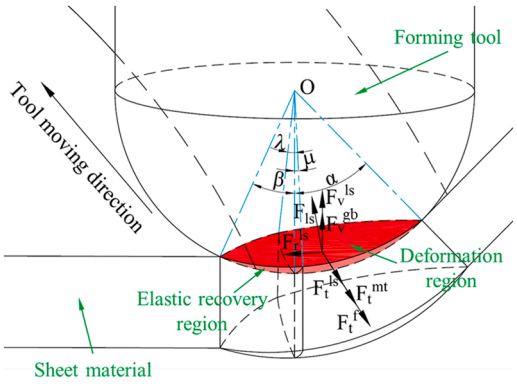

Fig. 6. Forming force components in ISF.

give the modelling method and to develop the analytical equations for calculation of forming forces in ISF.

The forming force (F) is decomposed to the vertical force (F_v) and horizontal force (F_h), between which the horizontal force may be comprised of the force in radial direction (F_r) and the force in tangential direction (F_t). As shown in Fig. 6, the vertical force may consist of the vertical component of localised shear force (F_v^{ls}) and the vertical force due to global bending (F_v^{gb}). The radial force F_r is perpendicular to the tool path and may come from the radial component of the localised shear force, while the tangential force F_t may be comprised of the localised shear force component in tangential direction (F_t^{ls}), the force leading to material thinning (F_t^{mt}) and the frictional force (F_t^f).

2.5.1. Vertical forming force related to local shear deformation

In ISF, the downward movement of material is driven by the forming tool. The tool may be seen as an indentation of the sheet along the normal direction of the contact region to generate deformation, and the sheet material gives a reaction force to oppose the tool movement and the material deformation. The vertical force is a combination of the vertical component of reaction shear force provided by the sheet material and the force resulting from the global bending.

According to the von-Mises yield criteria, in biaxial tension condition of the localised deformation region as indicated above, the shear stress τ may be calculated using the following equation (Hu et al., 2002):

$$\tau = \frac{1}{2} \bullet \sigma_s \tag{30}$$

where the yield stress σ_s is represented by σ_s^{P1}, σ_s^{P2}, σ_s^{P3}, σ_s^{P4} and σ_s^{P5} for different parts as shown in Fig. 2(c) and is calculated by the material constitutive model at the yield strain ε_s as given by Eq. (31), which may only come from the material thinning Δt after contact and deformation.

$$\varepsilon_s = 2 \bullet \ln\left[1 + \frac{\Delta t}{t_0 - \frac{t_0 \bullet (1-\cos\alpha) \bullet (\beta + \text{asin}\delta \bullet \cos\theta)}{\alpha+\beta}}\right] \tag{31}$$

where $\Delta t = t_0 \bullet (1-\cos\alpha) \bullet (\beta-\beta_1)/(\alpha+\beta)$ for P1, P2 and P5, while $\Delta t = t_0 \bullet (1-\cos\alpha) \bullet (\beta+\text{asin}\delta \bullet \cos\theta)/(\alpha+\beta)$ for P3 and P4. δ is represented by δ_{P1}, δ_{P2}, δ_{P3}, δ_{P4} and δ_{P5}, which are φ angles at boundaries of the five contact regions and are defined with different θ ranges by Eqs. (1), (4), (7) and (8).

The localised shear force (F_{ls}) in different contact regions may be calculated using the shear stress and through thickness area by the following expressions:

$$F_{ls}^{P1} = \int_0^{\frac{1}{2}\pi} \int_{r_{tool}}^{r_{tool}+t_{P1}} \frac{\sigma_s^{P1} \bullet \sin\delta_{P1} \bullet r_{tool}}{2 \bullet \cos\left[\frac{\pi}{2} - \theta - \arctan\left(\frac{b_{P1}{}^2 \bullet \cos\theta}{a_{P1}{}^2 \bullet \sin\theta}\right)\right]} \text{d}r\text{d}\theta \tag{32}$$

$$F_{ls}^{P2} = \int_{\frac{1}{2}\pi}^{\arccos\left(-\frac{\sin\beta_1}{\sin\beta}\right)} \int_{r_{tool}}^{r_{tool}+t_{P2}} \frac{\sigma_s^{P2} \bullet \sin\delta_{P2} \bullet r_{tool}}{2 \bullet \cos\left[\frac{\pi}{2} - \theta - \arctan\left(\frac{b_{P2}{}^2 \bullet \cos\theta}{a_{P2}{}^2 \bullet \sin\theta}\right)\right]} \text{d}r\text{d}\theta \tag{33}$$

$$F_{ls}^{P3} = \int_{\arccos\left(-\frac{\sin\beta_1}{\sin\beta}\right)}^{\pi} \int_{r_{tool}}^{r_{tool}+t_{P3}} \frac{\sigma_s^{P3} \bullet \sin\delta_{P3} \bullet r_{tool}}{2} \text{d}r\text{d}\theta \tag{34}$$

$$F_{ls}^{P4} = \int_{\pi}^{\frac{3}{2}\pi} \int_{r_{tool}}^{r_{tool}+t_{P4}} \frac{\sigma_s^{P4} \bullet \sin\delta_{P4} \bullet r_{tool}}{2 \bullet \cos\left[\frac{\pi}{2} + \theta + \arctan\left(\frac{b_{P4}{}^2 \bullet \cos\theta}{a_{P4}{}^2 \bullet \sin\theta}\right)\right]} \text{d}r\text{d}\theta \tag{35}$$

$$F_{ls}^{P5} = \int_{\frac{3}{2}\pi}^{2\pi} \int_{r_{tool}}^{r_{tool}+t_{P5}} \frac{\sigma_s^{P5} \bullet \sin\delta_{P5} \bullet r_{tool}}{2 \bullet \cos\left[\frac{\pi}{2} + \theta + \arctan\left(\frac{b_{P5}{}^2 \bullet \cos\theta}{a_{P5}{}^2 \bullet \sin\theta}\right)\right]} \text{d}r\text{d}\theta \tag{36}$$

where F_{ls}^{P1}, F_{ls}^{P2}, F_{ls}^{P3}, F_{ls}^{P4} and F_{ls}^{P5} are localised shear forces of P1, P2, P3, P4 and P5, respectively; t_{P1}, t_{P2}, t_{P3}, t_{P4} and t_{P5} are the thickness at the boundary of the five regions by Eqs. (13) and (14).

The vertical forming force due to localised shear force may be calculated using the following equation:

$$\begin{aligned} F_v^{ls} &= \cos\frac{\alpha-\beta}{2} \bullet \cos\frac{\lambda-\mu}{2} \bullet F_{ls} \\ &= \cos\frac{\alpha-\beta}{2} \bullet \cos\frac{\lambda-\mu}{2} \bullet \left(F_{ls}^{P1} + F_{ls}^{P2} + F_{ls}^{P3} + F_{ls}^{P4} + F_{ls}^{P5}\right) \end{aligned} \tag{37}$$

2.5.2. Vertical forming force from elastic deflection

Referring to the case of a circular plate, elastic deflection γ and concentrated force F_v^{gb} may have the following relationship:

$$\gamma = \frac{F_v^{gb} \bullet \left(R_b{}^2 - R^2\right)^2}{16 \bullet \pi \bullet D \bullet R_b{}^2} \tag{38}$$

where D in N·mm is the flexural rigidity of sheet material:

$$D = \frac{E \bullet t_0{}^3}{12 \bullet (1-\nu^2)} \tag{39}$$

where ν is the material Poisson's ratio. The part of vertical force from global bending can be expressed as follows:

$$F_v^{gb} = 16 \bullet \pi \bullet D \bullet \gamma \bullet \frac{R_b{}^2}{\left(R_b{}^2 - R^2\right)^2} \tag{40}$$

The global bending of the sheet material between the forming tool and the backing plate is totally recovered until the equivalent strain due to bending on the top surface (expressed as Eq. (41)) equals to the yield strain ε_s of the sheet material.

$$\bar{\varepsilon}_{gb} = \frac{2}{\sqrt{3}} \bullet \ln\frac{r_{gb} + t_0}{\sqrt{r_{gb} \bullet \left(r_{gb} + t_0\right)}} = \frac{1}{\sqrt{3}} \bullet \ln\frac{r_{gb} + t_0}{r_{gb}} \tag{41}$$

Therefore, when the elastic deflection reaches the maximum value, the bending has a critical radius as expressed by Eq. (42):

$$r_{gb}^{critical} = \frac{t_0}{\exp\left(\sqrt{3} \bullet \varepsilon_s\right) - 1} \tag{42}$$

According to the relationships given by Eqs. (20) and (21), the critical depth of tool position, i.e., the maximum elastic deflection can be derived and calculated by the following equation:

$$\begin{aligned} h_{critical} = &\left[\frac{t_0}{\exp\left(\sqrt{3} \bullet \varepsilon_s\right) - 1} + t_0 + r_{tool}\right] \\ &\bullet \left\{1 - \cos\left[\arcsin\frac{R_b - R}{\frac{t_0}{\exp\left(\sqrt{3} \bullet \varepsilon_s\right) - 1} + t_0 + r_{tool}}\right]\right\} \end{aligned} \tag{43}$$

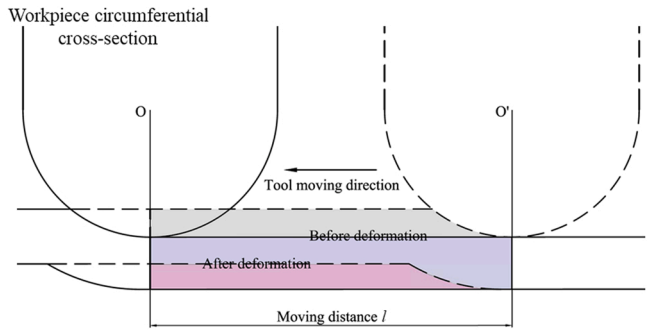

Fig. 7. Illustration of the workpiece circumferential cross-section before and after deformation with tool motion of distance l.

The elastic deflection γ equals to h until the tool position reaches a critical depth h_{critical}. After this position, the elastic deflection γ is treated as a constant value h_{critical}.

The vertical force is finally calculated as the superposition of F_{v}^{ls} and F_{v}^{gb} as following:

$$F_{\text{v}} = F_{\text{v}}^{\text{ls}} + F_{\text{v}}^{\text{gb}} \tag{44}$$

2.5.3. Horizontal forming forces

The horizontal forces in radial and tangential directions due to local shear behaviour have expressions as follows:

$$F_{\text{r}} = \sin\frac{\alpha-\beta}{2} \bullet \left(F_{\text{s}}^{\text{P1}} + F_{\text{s}}^{\text{P2}} + F_{\text{s}}^{\text{P3}} + F_{\text{s}}^{\text{P4}} + F_{\text{s}}^{\text{P5}}\right) \tag{45}$$

$$F_{\text{t}}^{\text{ls}} = \cos\frac{\alpha-\beta}{2} \bullet \sin\frac{\lambda-\mu}{2} \bullet \left(F_{\text{s}}^{\text{P1}} + F_{\text{s}}^{\text{P2}} + F_{\text{s}}^{\text{P3}} + F_{\text{s}}^{\text{P4}} + F_{\text{s}}^{\text{P5}}\right) \tag{46}$$

The derivation of the material thinning-related horizontal force is based on the energy method and the work done by the horizontal force in movement of l along the workpiece circumferential direction may lead to the thinning of the sheet, as shown in Fig. 7.

F_{t}^{mt} can be derived as the following expression:

$$F_{\text{t}}^{\text{mt}} = \int_0^{\beta}\int_{r_{\text{tool}}}^{r_{\text{tool}}+t_{\text{A}}} \overline{\sigma} \bullet r \bullet \overline{\varepsilon}^{\text{p}} \,\text{d}r\text{d}\varphi + \int_0^{\alpha}\int_{r_{\text{tool}}}^{r_{\text{tool}}+t_{\text{B}}} \overline{\sigma} \bullet r \bullet \overline{\varepsilon}^{\text{p}} \,\text{d}r\text{d}\varphi \tag{47}$$

In ISF, the cross-section shape of workpiece after deformation is determined by the meridional cross-section, which has the minimum area. Therefore, in this equation, the volume of the deformed material and the strain distribution are utilised on the workpiece meridional cross-section.

The frictional force F_{t}^{f} approximately has the following relationship with the vertical forming force:

$$F_{\text{t}}^{\text{f}} = f \bullet \left(F_{\text{ls}}^{\text{P1}} + F_{\text{ls}}^{\text{P2}} + F_{\text{ls}}^{\text{P3}} + F_{\text{ls}}^{\text{P4}} + F_{\text{ls}}^{\text{P5}}\right) \tag{48}$$

where f is the frictional coefficient between the forming tool and the sheet. The tangential, horizontal and total forces, F_{t}, F_{h} and F can be calculated as following:

$$F_{\text{t}} = F_{\text{t}}^{\text{ls}} + F_{\text{t}}^{\text{mt}} + F_{\text{t}}^{\text{f}} \tag{49}$$

$$F_{\text{h}} = \sqrt{{F_{\text{t}}}^2 + {F_{\text{r}}}^2} \tag{50}$$

$$F = \sqrt{{F_{\text{v}}}^2 + {F_{\text{h}}}^2} \tag{51}$$

2.6. Forming force in biaxial tension condition area

At the corner of ISF formed parts, the material deformation at global level presents biaxial tension condition (Park and Kim, 2003), which causes the sudden change of contact region, deformation state and forming force. As shown in Fig. 3(e) and (f), the strain components along the corner positions of truncated pyramid parts also show the distribution relationship in the biaxial tension condition, which is distinguished from the plane strain condition. This section presents the analytical modelling of forming force in biaxial tension condition area by adapting the modelling method in Sections 2.1–2.5.

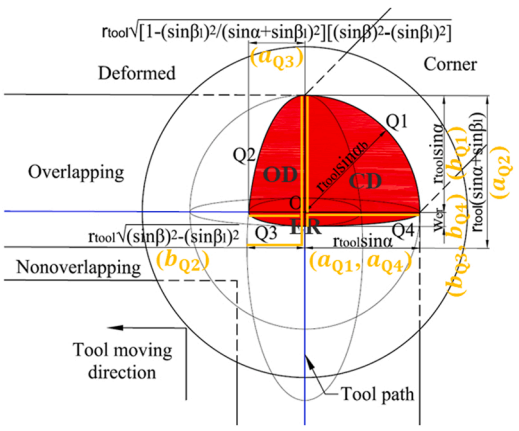

Fig. 8. Illustration of contact region (red colour) on forming tool surface in biaxial tension condition at corner from top view.

2.6.1. Contact region

As shown in Fig. 1(e) and (f), the blue area represents the contact region at the corner in end milling process or ISF process of a rigid plastic material. In consideration of the elastic deformation before contact and the recovery after contact in ISF, a shrink and an expansion are applied to the front and rear contact regions, respectively, as illustrated by the white borders.

In biaxial tension condition area, the contact region may be comprised of four different parts: corner deformation (CD) region, overlapping deformation (OD) region and elastic recovery (ER) region, each of which can be assumed as a part of elliptical or super elliptical shape as shown in Fig. 8. The boundaries of CD and OD regions are represented by Q1 and Q2, respectively, while the boundary of ER region consists of Q3 and Q4.

The lateral edge of the pyramid is defined as the intersecting line between two lateral faces, and the drawing angle α_{b} becomes slightly smaller when the tool moves to the corner. Therefore, Q1 can be considered as a part of super ellipse, and the semi-major and semi-minor axes are $a_{\text{Q1}} = b_{\text{Q1}} = r_{\text{tool}} \bullet \sin\alpha$. In the spherical coordinate system, given that $(r_{\text{tool}}, \alpha_{\text{b}}, \pi/4)$ is on the super ellipse, the boundary of Q1 can be expressed as the following equation by projecting the super ellipse in the horizontal plane to the hemispherical tool surface:

$$\left|\frac{r_{\text{tool}} \cdot \sin\varphi \cdot \cos\theta}{a_{\text{Q1}}}\right|^{\ln\frac{1}{2}} \Big/ \ln\frac{\sin\alpha_{\text{b}}}{\sqrt{2}\cdot\sin\alpha} + \left|\frac{r_{\text{tool}} \cdot \sin\varphi \cdot \sin\theta}{b_{\text{Q1}}}\right|^{\ln\frac{1}{2}} \Big/ \ln\frac{\sin\alpha_{\text{b}}}{\sqrt{2}\cdot\sin\alpha} = 1 \tag{52}$$

With semi-major and semi-minor axes of $a_{\text{Q2}} = r_{\text{tool}} \bullet (\sin\alpha + \sin\beta_1)$ and $b_{\text{Q2}} = r_{\text{tool}} \bullet \sqrt{(\sin\beta)^2 - (\sin\beta_1)^2}$, the elliptical boundary of Q2 can be given by the following equation:

$$\frac{(r_{\text{tool}} \bullet \sin\varphi \bullet \cos\theta)^2}{{b_{\text{Q2}}}^2} + \frac{(r_{\text{tool}} \bullet \sin\varphi \bullet \sin\theta + r_{\text{tool}} \bullet \sin\beta_1)^2}{{a_{\text{Q2}}}^2} = 1 \tag{53}$$

With semi-major and semi-minor axes of $a_{\text{Q3}} = r_{\text{tool}} \bullet \sqrt{\left[1 - \frac{(\sin\beta_1)^2}{(\sin\alpha+\sin\beta_1)^2}\right] \bullet \left[(\sin\beta)^2 - (\sin\beta_1)^2\right]}$ and $b_{\text{Q3}} = w_{\text{er}}$, the elliptical boundary of Q3 can be expressed as:

$$\frac{(r_{\text{tool}} \bullet \sin\varphi \bullet \cos\theta)^2}{{a_{\text{Q3}}}^2} + \frac{(r_{\text{tool}} \bullet \sin\varphi \bullet \sin\theta)^2}{{b_{\text{Q3}}}^2} = 1 \tag{54}$$

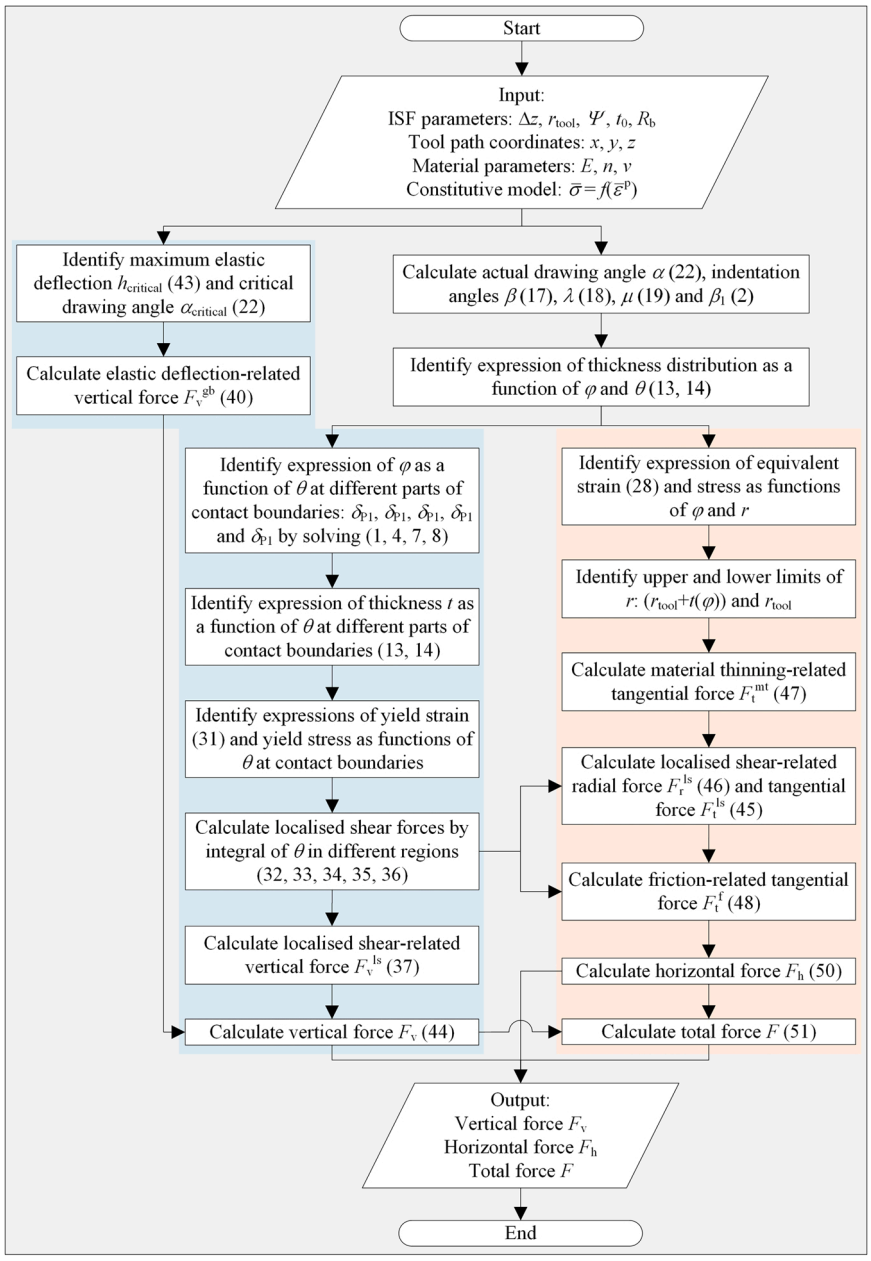

Fig. 9. Flow chart to solve and implement the analytical model of forming force prediction in plane strain condition in ISF.

Finally, with semi-major and semi-minor axes of $a_{Q4} = r_{tool} \bullet \sin\alpha$ and $b_{Q4} = w_{er}$, the expression of the elliptical boundary of Q4 is derived as the following:

$$\frac{(r_{tool} \bullet \sin\varphi \bullet \cos\theta)^2}{{a_{Q4}}^2} + \frac{(r_{tool} \bullet \sin\varphi \bullet \sin\theta)^2}{{b_{Q4}}^2} = 1 \tag{55}$$

2.6.2. Vertical forming force

Referring to plane strain condition area, the vertical force in biaxial tension condition area can be derived as in the following expression:

$$F_v = \cos\frac{\alpha_b}{2} \bullet \left(F_{ls}^{Q1} + F_{ls}^{Q2} + F_{ls}^{Q3} + F_{ls}^{Q4}\right) + F_v^{ed} \tag{56}$$

where $F_{ls}^{Q2} = F_{ls}^{P1}$, $F_{ls}^{Q4} = F_{ls}^{P5}$ and F_{ls}^{Q3} can be approximated as F_{ls}^{P4}. F_{ls}^{Q1} can be calculated by the following equation:

$$F_{ls}^{Q1} = \int_0^{\frac{1}{2}\pi} \int_{r_{tool}}^{r_{tool}+t_{Q1}} \frac{\sigma_s^{Q1} \cdot \sin\delta_{Q1} \cdot r_{tool}}{2 \cdot \cos\left\{\frac{\pi}{2} - \theta - \arctan\left[(\cot\theta)^{\ln\frac{1}{2} \Big/ \ln\frac{\sin\alpha_b}{\sqrt{2}\cdot\sin\alpha} - 1}\right]\right\}} \mathrm{d}r\mathrm{d}\theta \tag{57}$$

where t_{Q1} and σ_s^{Q1} are the sheet thickness and the yield stress of Q1, respectively. The sheet thickness at the immediate proximity near the contact region at the corner can be approximated as $t_0 \bullet \cos\alpha_b$. According to the assumption of linear distribution, when $0 \le \theta \le \frac{\pi}{4}$, the expression of t_{Q1} can be given by the following equation:

$$t_{Q1} = t_0 \bullet \cos\alpha + t_0 \bullet (\cos\alpha_b - \cos\alpha) \bullet \frac{4 \bullet \theta}{\pi} \tag{58}$$

When $\frac{\pi}{4} \le \theta \le \frac{\pi}{2}$, the thickness distribution along Q1 has the following expression:

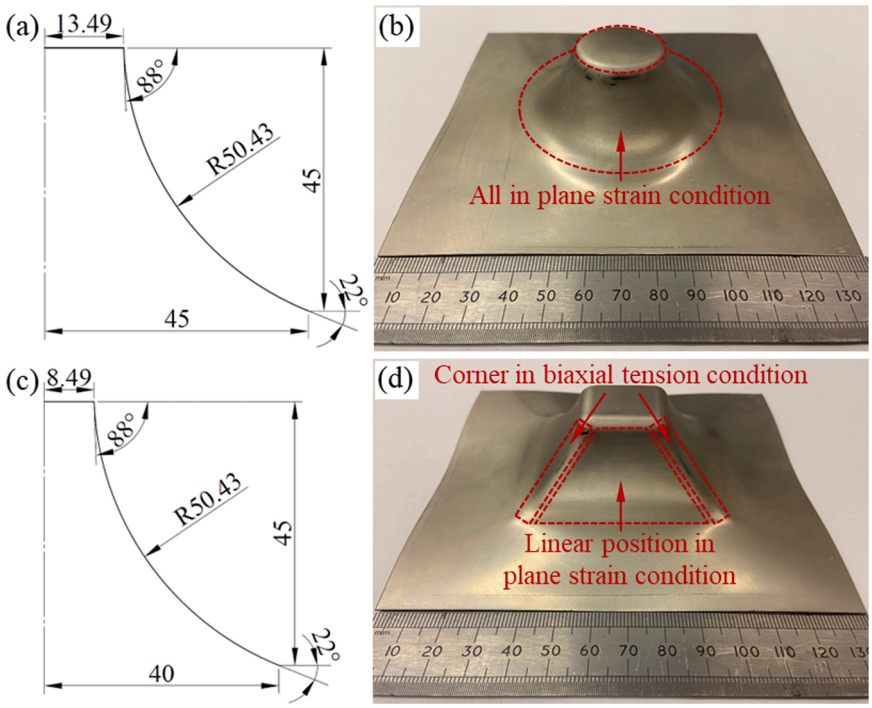

Fig. 10. Designed profiles and formed ISF parts in (a), (b) truncated cone shape, and (c), (d) truncated pyramid shape with varying drawing angle for experimental validation of forming forces.

$$t_{Q1} = t_0 \bullet \cos\alpha_b - t_0 \bullet (\cos\alpha_b - \cos\alpha) \bullet \frac{4 \bullet \theta - \pi}{\pi} \tag{59}$$

σ_s^{Q1} in Eq. (57) may be calculated at the yield strain ε_s^{Q1} as following by referring to Eq. (31):

$$\varepsilon_s^{Q1} = 2 \bullet \ln\left(1 + \frac{\Delta t_{Q1}}{t_{Q1}}\right) \tag{60}$$

where Δt_{Q1} is the thickness reduction of Q1 after contact and $\Delta t_{Q1} = t_0 \bullet (1 - \cos\alpha_b) \bullet (\beta_b - \beta_{1b})/(\alpha_b + \beta_b)$. β_b and β_{1b} are the β angle and β_1 angle at the corner, respectively, and $\beta_b = \text{asin}(\sin\beta/\cos 45^\circ)$, $\beta_{1b} = \text{asin}(\sin\beta_1/\cos 45^\circ)$.

Therefore, F_{ls}^{Q1} can be calculated by putting Eqs. (58)–(60) in Eq. (57) and the vertical forming force F_v can be calculated by Eq. (56).

2.6.3. Horizontal forming force

In biaxial tension condition, the influence of ND region on the decomposition of localised shear force can be neglected as it is much smaller than CD region. Therefore, the tangential force is only comprised of the force related to material thinning and the frictional force. Referring to the calculation method in plane strain condition area, the tangential horizontal force related to material thinning in biaxial tension condition can be derived as in the following equation:

$$F_t^{mt} = \int_0^{\alpha_b} \int_{r_{tool}}^{r_{tool}+t_b} \overline{\sigma} \bullet r \bullet \overline{\varepsilon}^p \mathrm{d}r\mathrm{d}\varphi \tag{61}$$

where t_b is the thickness distribution along the workpiece meridional direction in biaxial tension condition at corner, and t_b has the following expression:

$$t_b = t_0 - \frac{t_0 \bullet (1 - \cos\alpha) \bullet \beta}{\alpha + \beta} + \left[t_0 - \frac{t_0 \bullet (1 - \cos\alpha) \bullet \beta}{\alpha + \beta} - t_0 \bullet \cos\alpha_b\right] \bullet \frac{\varphi}{\alpha_b} \tag{62}$$

Besides, the frictional force F_t^f and the horizontal force in the radial direction F_r can be derived and approximated as the following equations:

$$F_t^f = f \bullet \left(F_s^{Q1} + F_s^{Q2} + F_s^{Q3} + F_s^{Q4}\right) \tag{63}$$

$$F_r = \sin\frac{\alpha_b}{2} \bullet \left(F_s^{Q1} + F_s^{Q2} + F_s^{Q3} + F_s^{Q4}\right) \tag{64}$$

The horizontal force and total forming force in biaxial tension condition can be calculated by Eqs. (50) and (51), respectively.

2.7. Implementation

MATLAB software is used to implement and visualise the derived analytical model of force prediction, and the implementation steps are given in the flow chart as shown in Fig. 9, where the calculation method for the plane strain condition area is introduced. In the flow chart shown in Fig. 9, the equations used for each step are indicated for convenience.

3. Force prediction and validation

This section presents the validation of the new analytical model using two materials: a titanium alloy TA1 and an aluminium alloy AA1003 at different deformation conditions (plane strain and biaxial tension conditions) with different process parameters (step size, tool dimension, drawing angle and sheet thickness). Validation is also given by the force prediction in a practical application of ISF-based cranial plate manufacture. At last, this section gives a comparison between the developed analytical model and other representative models.

3.1. Model validation from ISF of TA1 sheet

In the developed analytical model, two different conditions are considered in ISF: plane strain condition on the flat surface and biaxial tension condition at the corner. This section aims to validate the

Table 1
Johnson-Cook parameters of TA1 and AA3003-O sheet.

Material	A (MPa)	B (MPa)	n	E (MPa)
TA1	220.6	341.3	0.4692	105,000
AA3003-O	41.37	79.22	0.2244	68,900

analytical model with two different forming shapes designed and formed as shown in Fig. 10. The drawing angles of the designed parts vary from 22° to 88° and the forming forces during ISF of 140 × 140 × 0.7 mm TA1 sheet were measured. Step size in ISF of the truncated cone is 0.28 mm, while for ISF of the truncated pyramid it is 0.44 mm. Other process parameters are the same: with tool radius of 5 mm, feed rate of 800 mm/min, no spindle rotation, and with use of RTD COMPOUND lubricant.

Table 2
Horizontal force conversion in ISF of truncated cone and pyramid parts.

Tool position conditions		F_x	F_y
All positions of truncated cone part		$\frac{y}{\sqrt{x^2+y^2}}\bullet F_t - \frac{x}{\sqrt{x^2+y^2}}\bullet F_r$	$-\frac{x}{\sqrt{x^2+y^2}}\bullet F_t - \frac{y}{\sqrt{x^2+y^2}}\bullet F_r$
Linear positions of truncated pyramid part	$\left\|\frac{y}{x}\right\| < 1 \ \& \ x > 0$	$-F_r$	$-F_t$
	$\left\|\frac{y}{x}\right\| < 1 \ \& \ x < 0$	F_r	F_t
	$\left\|\frac{y}{x}\right\| > 1 \ \& \ y > 0$	F_t	$-F_r$
	$\left\|\frac{y}{x}\right\| > 1 \ \& \ y < 0$	$-F_t$	F_r
Corner positions of truncated pyramid part	$\frac{y}{x} = 1 \ \& \ x > 0$	$\frac{\sqrt{2}}{2}\bullet(F_t - F_r)$	$-\frac{\sqrt{2}}{2}\bullet(F_t + F_r)$
	$\frac{y}{x} = 1 \ \& \ x < 0$	$-\frac{\sqrt{2}}{2}\bullet(F_t - F_r)$	$\frac{\sqrt{2}}{2}\bullet(F_t + F_r)$
	$\frac{y}{x} = -1 \ \& \ y > 0$	$\frac{\sqrt{2}}{2}\bullet(F_t + F_r)$	$\frac{\sqrt{2}}{2}\bullet(F_t - F_r)$
	$\frac{y}{x} = -1 \ \& \ y < 0$	$-\frac{\sqrt{2}}{2}\bullet(F_t + F_r)$	$-\frac{\sqrt{2}}{2}\bullet(F_t - F_r)$

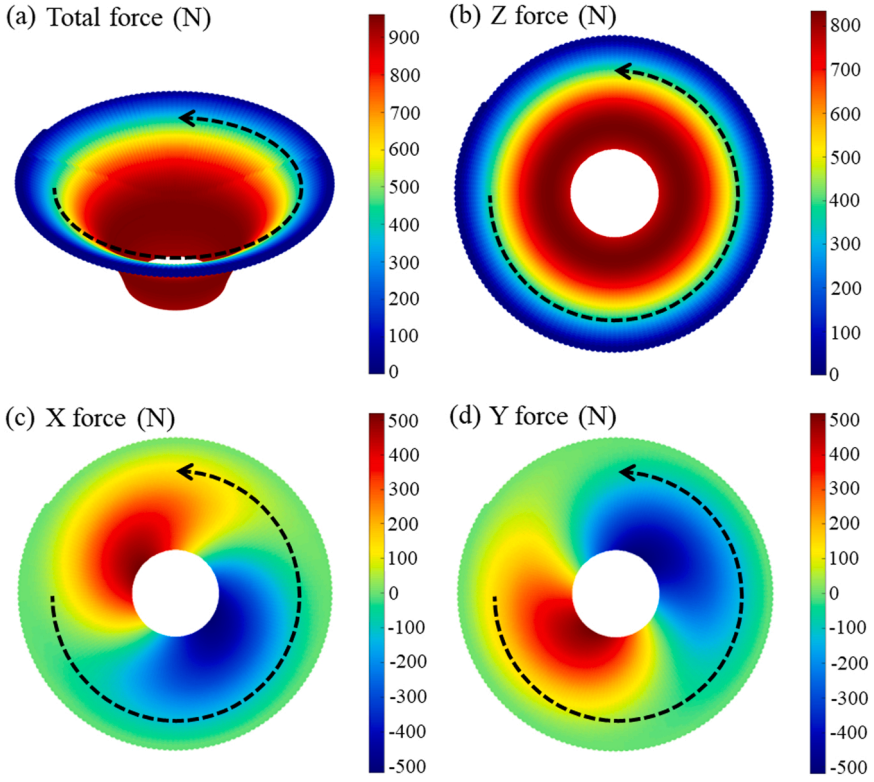

Fig. 11. Contour plots for analytically predicted results of (a) total force, (b) z force, (c) x force and (d) y force of different tool position in ISF of truncated cone part of TA1.

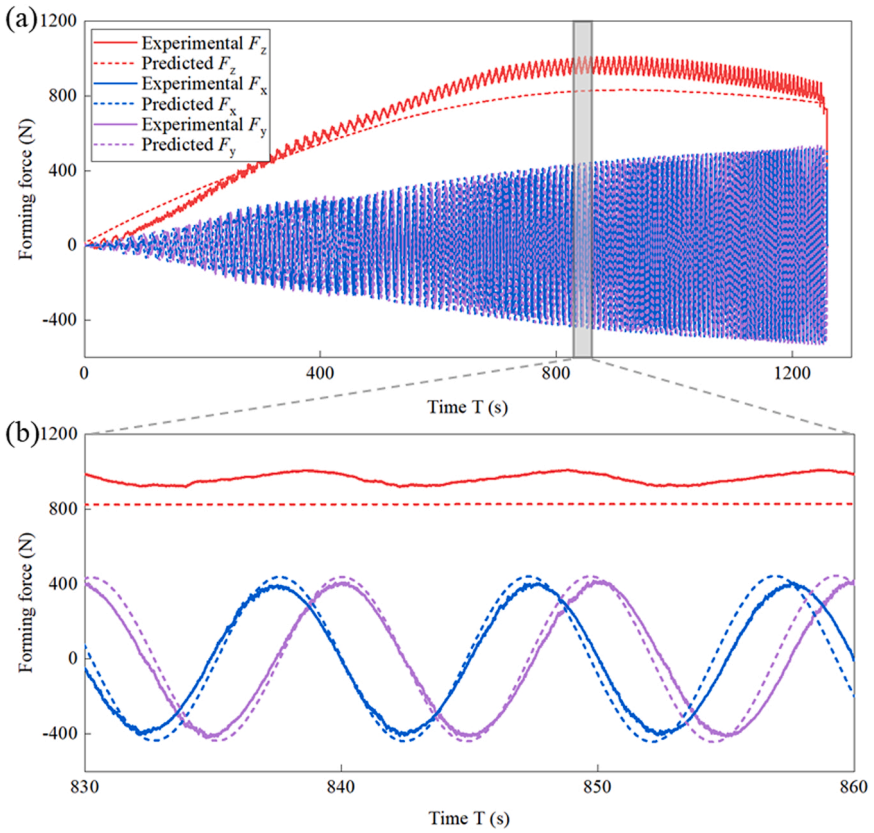

Fig. 12. Comparison between experimental (solid curves) and analytically predicted (dashed curves) force components in ISF of truncated cone part of TA1: (a) whole process comparison and (b) detailed comparison in an enlarged time range from 830 s to 860 s.

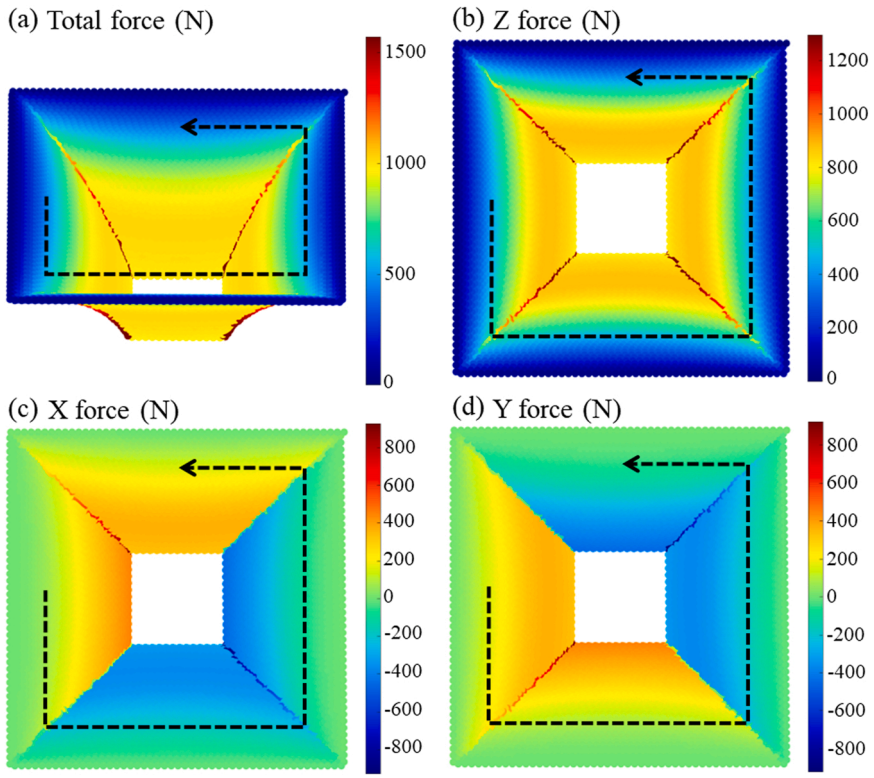

Fig. 13. Contour plot for analytically predicted results of (a) total force, (b) z force, (c) x force and (d) y force of different tool position in ISF of truncated pyramid part of TA1.

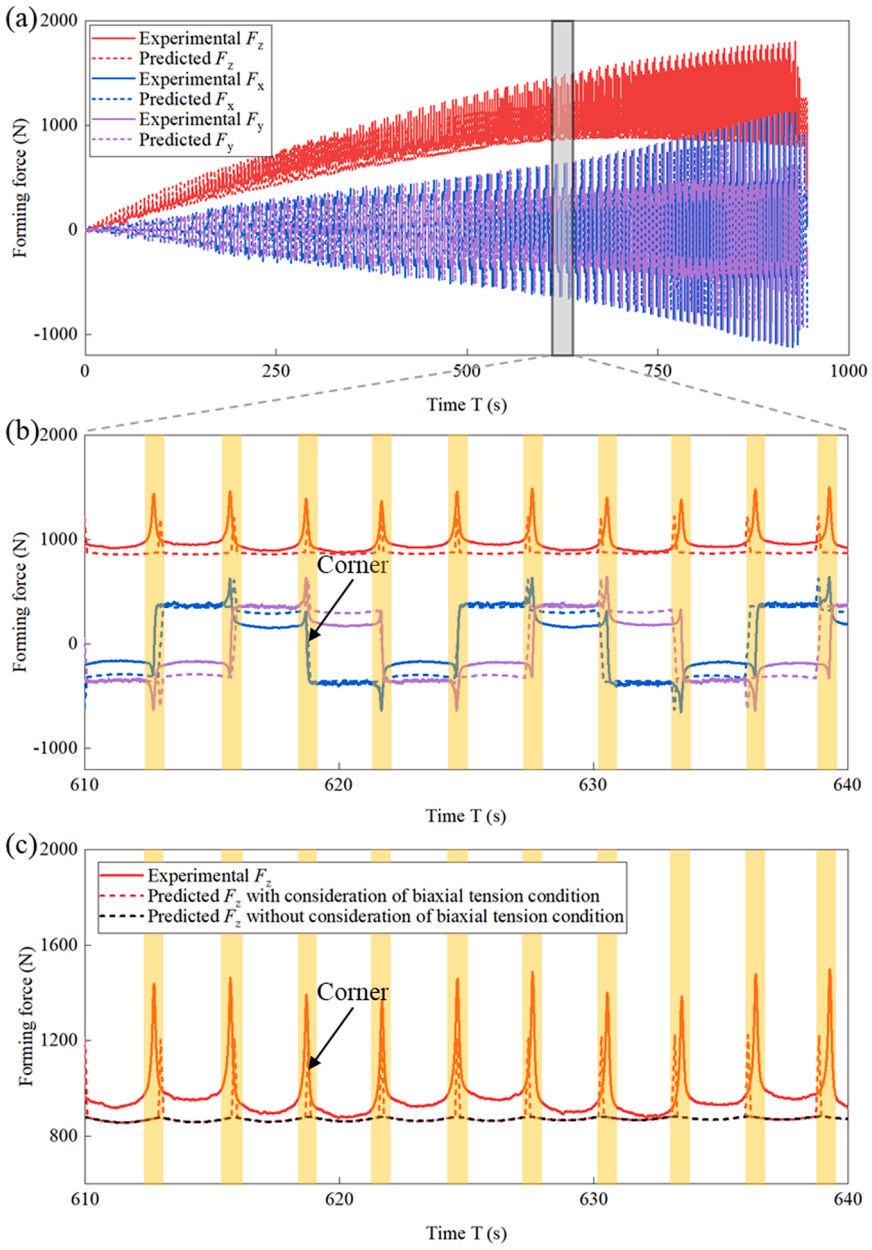

Fig. 14. Comparison between experimental (solid curves) and analytically predicted (dashed curves) force components in ISF of truncated pyramid part of TA1: (a) whole process comparison, (b) detailed comparison in an enlarged time range from 610 s to 640 s and (c) prediction with (red dashed curve) and without (black dashed curve) consideration of biaxial tension condition.

Frictional coefficient of 0.25 is used, and Johnson-Cook model as given by Eq. (65) is applied to describe the constitutive behaviour. The model parameters given in Table 1 were based on the quasi-static uniaxial tensile test. As the effects of strain rate and temperature are not considered in the current model, the constitutive model only has the part to predict the flow stress at different equivalent plastic strain.

$$\overline{\sigma} = A + B * (\overline{\varepsilon}^{p})^{n} \tag{65}$$

In ISF processing of the designed regular shapes, the prediction of forming force in x, y, and z axes of the ISF machine may be more convincing in the validation. Therefore, z force (F_z), x force (F_x) and y force (F_y) are predicted and compared with experimental results. F_z equals to F_v in the derivation, while F_x and F_y at different tool positions are converted from the tangential (F_t) and radial forces (F_r) by the rules in Table 2.

The prediction results of total force and force components during the motion of forming tool are presented in Fig. 11. For convenience, the force variation with the change of tool position is given in a contour plot. Different colours indicate the predicted force levels when the tool moves to different positions. Fig. 10(a) and (b) shows the nonuniform distribution of rising total and z forces with the increase of forming depth. This is due to the change of drawing angle and the relatively uniform force distribution in the same or adjacent tool path layers. Meanwhile, as given by Fig. 10(c) and (d), horizontal forces in x and y axes are in regular alternant variation because of the approximate circular tool path.

The comparison of force components over time between analytical prediction and experimental results is presented in Fig. 12. The gradual increase of all force components is due to the increase of draw angle and the same trend of x and y force fluctuation give an indication of the same deformation behaviour and contact condition in ISF of truncated cone part. The slight fluctuation may come from the non-horizontal

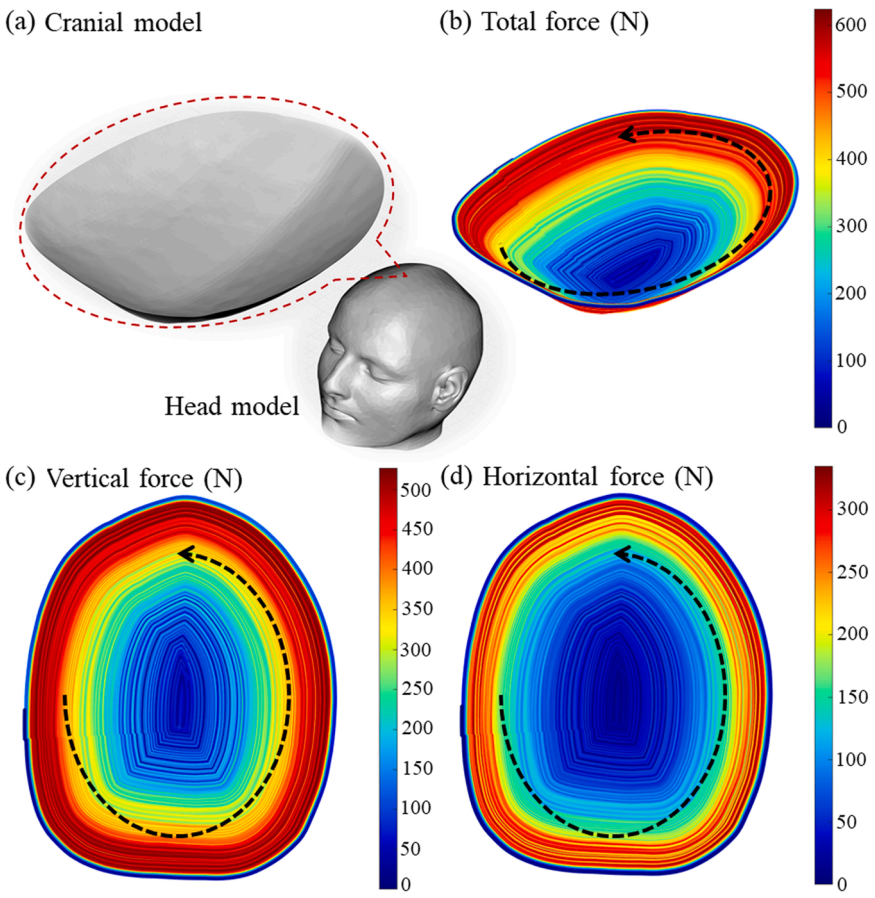

Fig. 15. Application of the analytical model in ISF-based manufacture of cranial plate: (a) Head and cranial models, (b) contour plot for prediction of total force, (c) contour plot for prediction of vertical force, (d) contour plot for prediction of horizontal force.

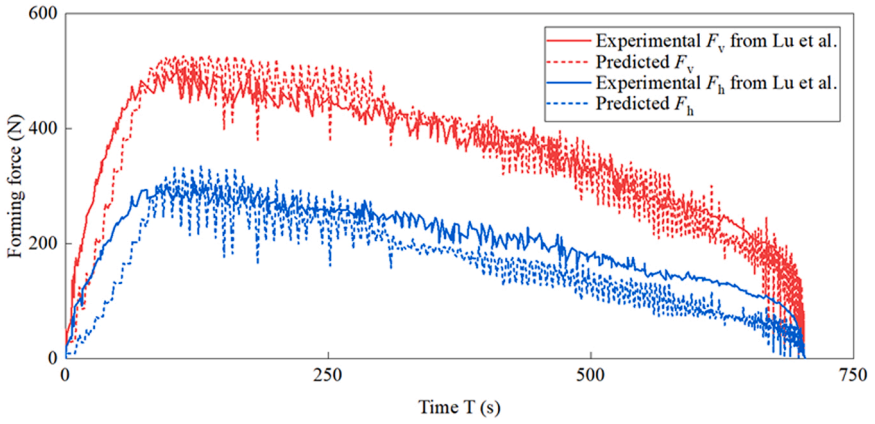

Fig. 16. Comparison between the experimental vertical force F_v and horizontal force F_h (solid curves) from Lu et al. (2016) and the analytically predicted results (dashed curves) in ISF-based manufacture of cranial plate.

placement of the ISF fixture, the stiffness change of sheet material (Chang et al., 2019), or the effect of the anisotropy. The comparison shows that the prediction is in good agreement with experiment and the predicted z force has a smooth variation trend because of the unchanged deformation behaviour and contact condition in the model implementation. As shown in Fig. 12(b), the detailed force variation in an enlarged time range from 830 s to 860 s further indicates the prediction accuracy and confirms the regular alternant variation of x and y forces.

As shown in Fig. 13, the predicted force distribution in ISF of truncated pyramid part shows that the force gradually increases when the tool moves from the middle position of linear part to the corner as well as with the increase of forming depth/drawing angle. A dramatic increase of total force and force components is presented at the corner, where the calculation follows the analysis and equations for biaxial tension condition area. The alternant variation can also be predicted in the distribution of x and y forces.

As shown by the solid curves in Fig. 14, experimental z, x, and y force signals have significant fluctuation. Each time when the tool moves to the corner, the force would increase dramatically, which results from the sudden change of deformation behaviour and the enhanced tool-sheet

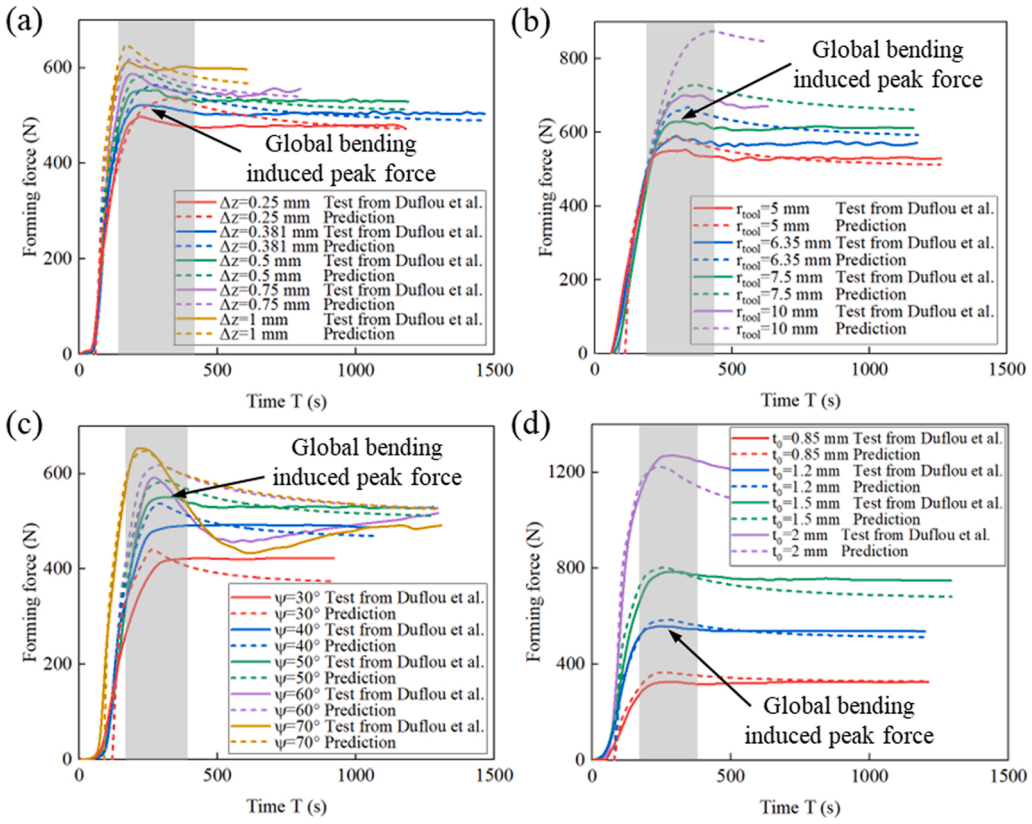

Fig. 17. Experimental total force (solid curves) from Duflou et al. (2007a) and predicted total force (dashed curves) in ISF of AA3003-O with different (a) step size from 0.25 mm to 1 mm, (b) tool radius from 5 mm to 10 mm, (c) drawing angle from 30° to 70° and (d) sheet thickness from 0.85 mm to 2 mm.

contact. However, at the linear part of pyramid, the z force is comparable to that of truncated cone but only has some more frequent fluctuation. This clarifies that the deformation behaviour and contact condition at the linear part of the pyramid are the same as the truncated cone. The periodic fluctuation from the middle position of linear part to the position near the corner is a result of the slight change in bending condition, which affects the actual drawing angle.

As shown in Fig. 14(a) and (b), the comparison between predicted and experimental results shows a good correlation, no matter at linear or corner positions, in vertical or horizontal components. To further confirm the model validity and the prediction effect, only the model for plane strain condition area is used to predict the force in whole process. As presented by the dashed black curve in Fig. 14(c), there is no sudden increase in z force but only slight fluctuation. This proves that, without the analytical modelling in biaxial tension condition area, the model is not able to predict the dramatic force change at the corner but can only describe the bending effect. This demonstrates that the analytical model successfully differentiates the force prediction for either plane strain or biaxial tension condition areas and clarifies that the remarkable fluctuation is mainly caused by the change of deformation mode and contact condition. By considering the effects of deformation condition, changed contact area and global bending, the analytical model shows the capability in predicting force variations and presenting the force characterisation accurately of different components.

3.2. Model validation in a practical application

To broaden the application of the analytical model, ISF-based manufacture of a cranial plate is used in this section for further validation. As shown in Fig. 15(a), the cranial plate, which is a customised asymmetric shape, was manufactured by ISF of 0.5 mm thickness TA1 sheet (Lu et al., 2016). The vertical and horizontal forces during the manufacture process were measured by Lu et al. (2016). The analytical prediction results of forming forces are given in Fig. 15(b)–(d).

Fig. 15(b)–(d) presents the contour plot of the total, vertical and horizontal force variations, which has a sharp increase at the beginning and a gradual decreasing trend when the tool moves towards the part centre. This is also confirmed by Fig. 16, where the solid and dashed curves represent experimental and analytical results, respectively. As shown by the red and blue dashed curves, the vertical and horizontal forces can be predicted with high accuracy. Moreover, the analytical model is effective to reflect the fluctuation, which is caused by drawing angle variation at the same layer and step size changes between each layer due to the irregular cranial shape. It is noteworthy that the prediction of vertical force is totally determined with the predefined process parameters in tool path generation. However, the prediction accuracy of horizontal force partially depends on the coefficient of friction, which is an unknown factor even if the lubrication type is given. A value of 0.25 is used as the coefficient of friction in this analytical prediction. The effect of lubrication condition and frictional coefficient on the prediction results is discussed in Section 4.1.

3.3. Model validation from ISF of AA1003-O sheet

The ISF testing results of AA3003-O by Duflou et al. (2007a) are used to validate the developed model in this section. The tests of truncated cone parts were carried out with different parameters, and the base test had step size of 0.5 mm, tool radius of 5 mm, drawing angle of 50° and sheet thickness of 1.2 mm. The constitutive behaviour of AA3003-O is still described by Johnson-Cook model, parameters of which were derived based on the published test (Hagan and Jeswiet, 2003) and can be found in Table 1.

The predicted total force and the comparison with experimental results are given in Fig. 17. The variation follows the same trend: at initial

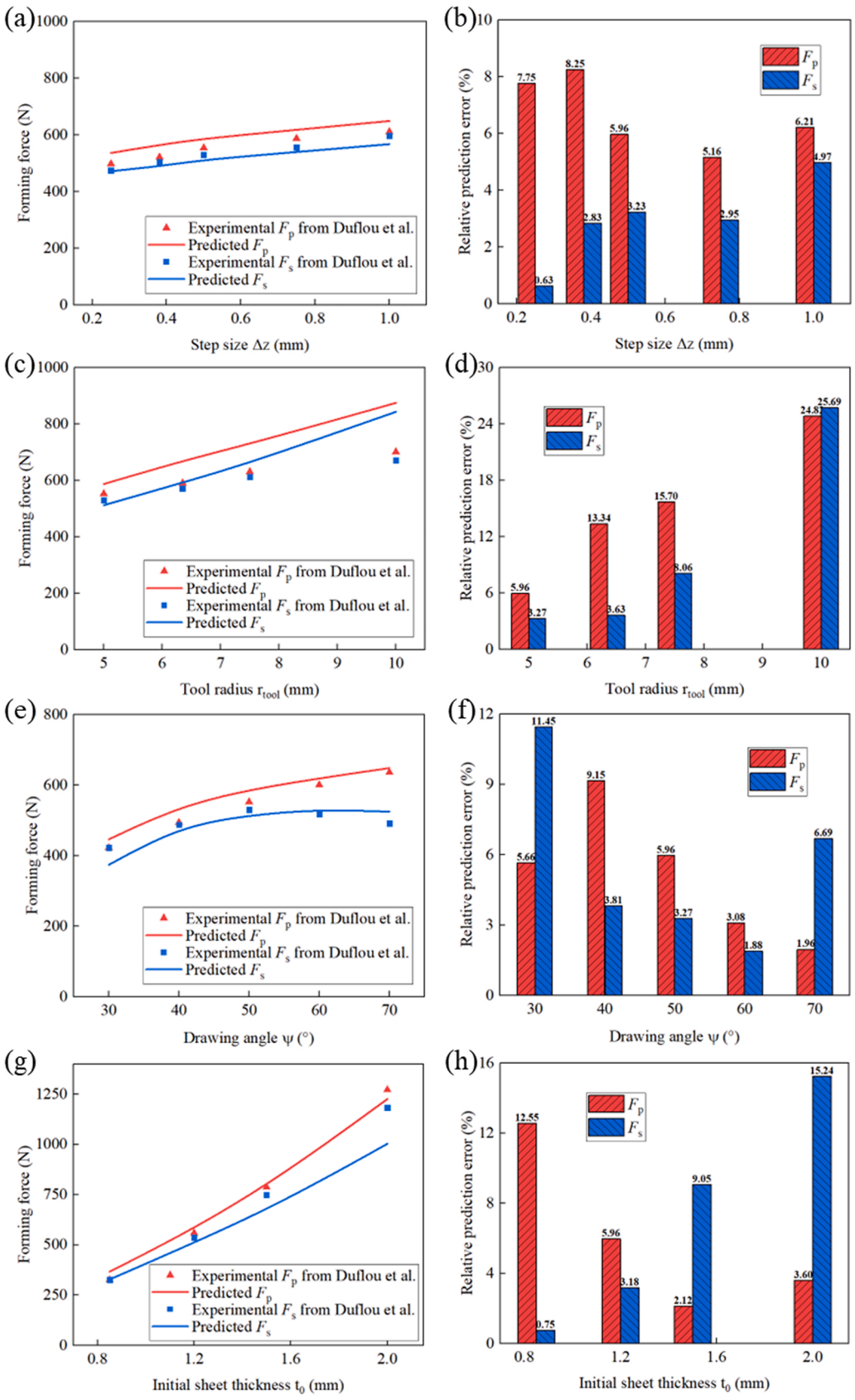

Fig. 18. Comparison of peak F_p and stabilised forces F_s between experimentally measured results from Duflou et al. (2007a) and analytically predicted results in ISF of AA3003-O with different (a) step size, (c) tool radius, (e) drawing angle and (g) sheet thickness.

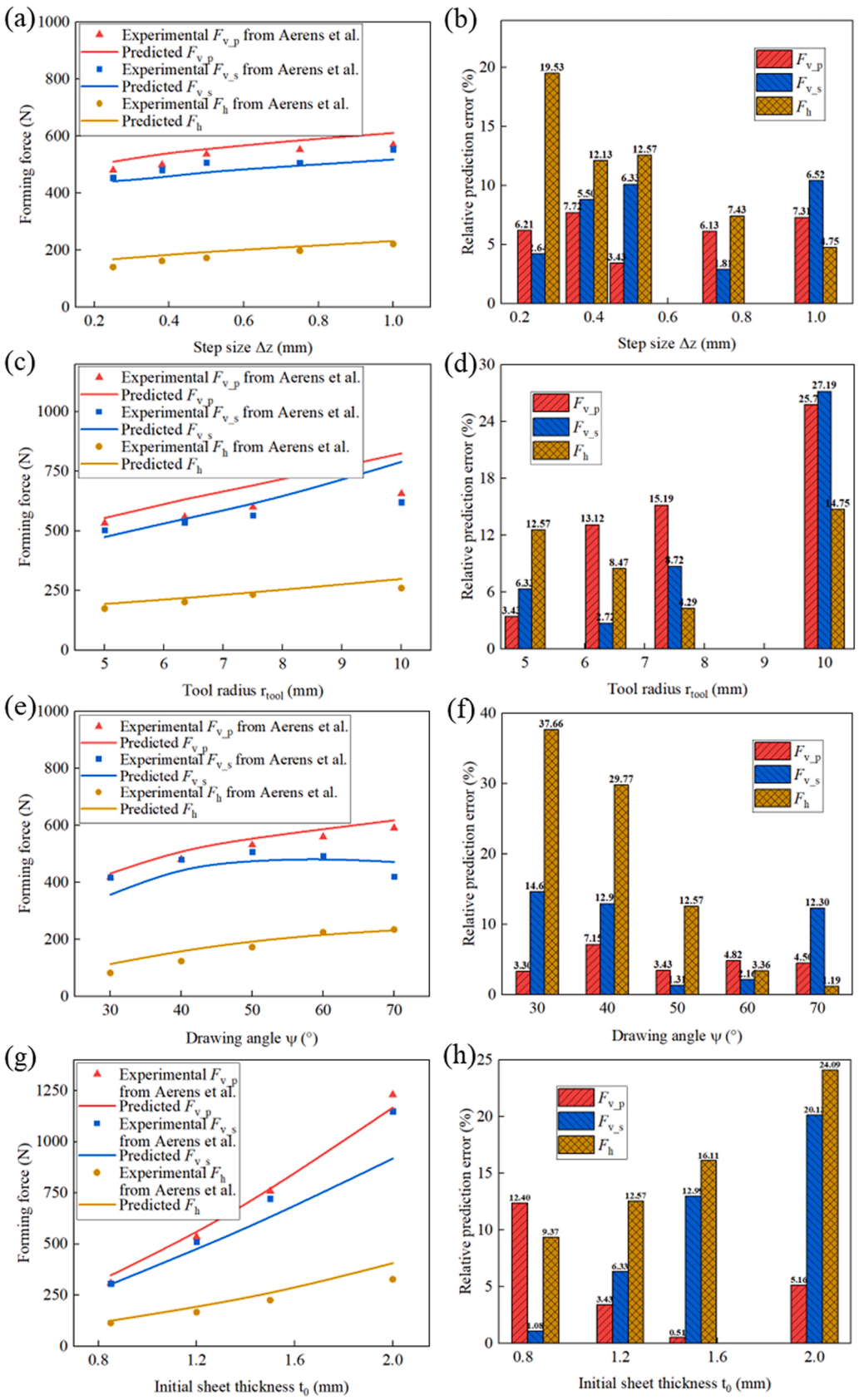

Fig. 19. Comparison of force components between experimentally measured results from Aerens et al. (2010) and analytically predicted results in ISF of AA3003-O with different (a) step size, (c) tool radius, (e) drawing angle and (g) sheet thickness.

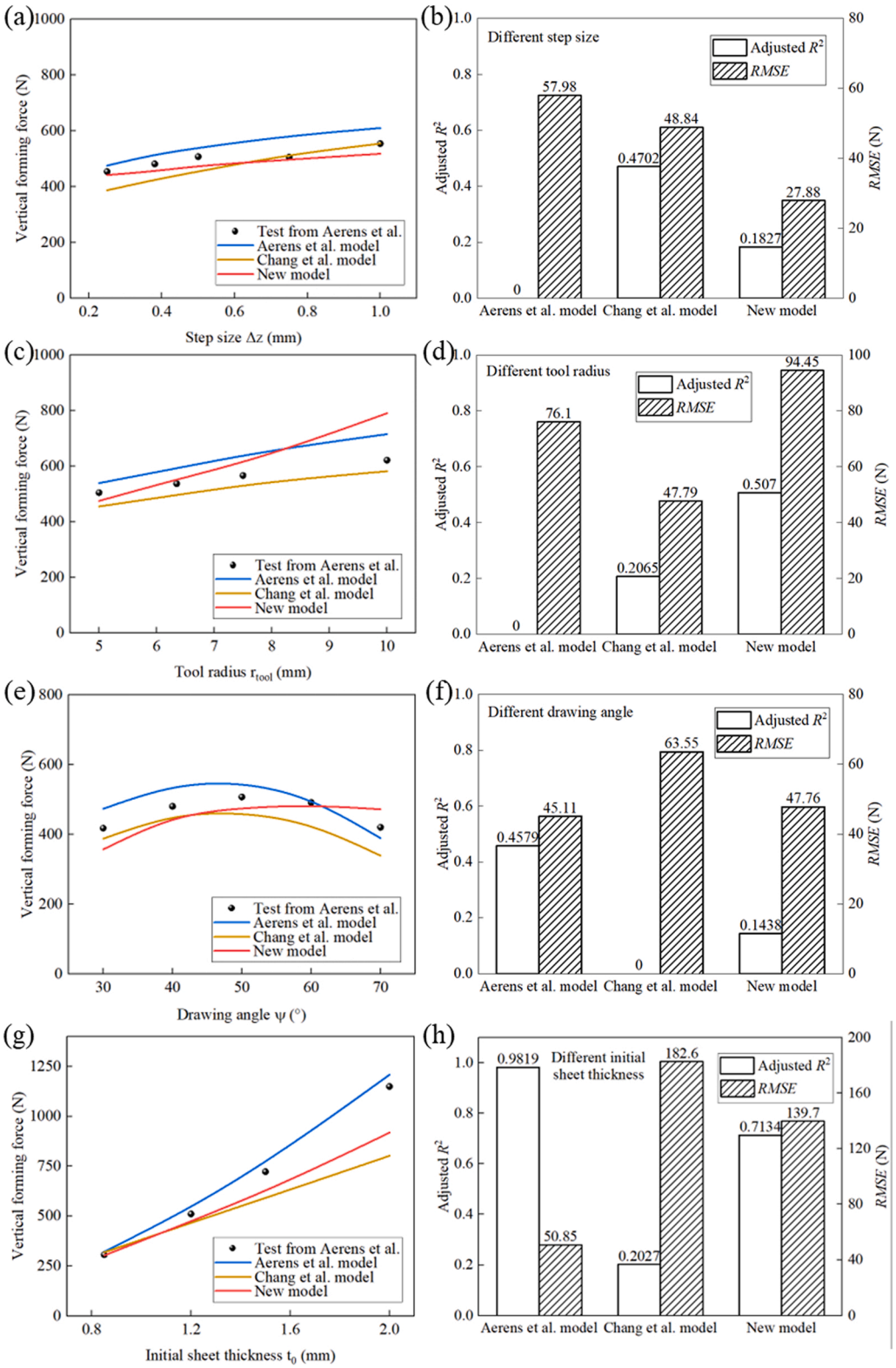

Fig. 20. Comparisons with R^2_{adj} and *RMSE* of vertical forming force predicted by Aerens et al., Chang et al. and the new models at different (a), (b) step size, (c), (d) tool radius, (e), (f) drawing angle and (g), (h) sheet thickness based on testing results in ISF of AA3003-O by Aerens et al. (2010).

stage, the forming force continuously increases until a global bending induced peak force (F_p) is reached, and after the peak, a reduction of forming force occurs followed by stabilised force (F_s) afterwards. For different parameters, the predicted results of the analytical model can describe the varying trend well.

As shown in Fig. 17(a), both experimental and predicted results show that with the increase of step size, larger forming force are obtained. Fig. 17(b) shows that larger tool radius increases forming force obviously, and with the increase of tool dimension, worse prediction effect is observed. In terms of different drawing angle, experimental results show

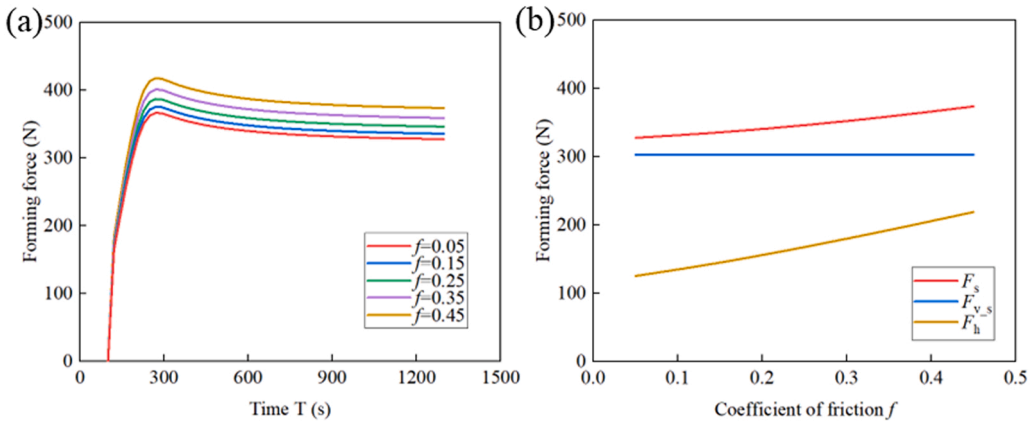

Fig. 21. Effect of frictional coefficient on (a) forming force history and (b) stabilised total force F_s, stabilised vertical force F_{v_s} and horizontal force F_h.

that the peak force only appears when the drawing angle is larger than 50°. For the analytical results in dashed lines, the peak force exists at all drawing angles, but the peak becomes slightly less obvious at smaller drawing angles. It is noteworthy that at large drawing angles of 60° and 70°, the experimental curve presents an obvious trough after peak. This may be caused by the sheet material wear (Ambrogio et al., 2006), which is not included in the modelling, so the predicted curve cannot reflect the corresponding effect. Finally, with the increase of sheet thickness, the forming force is increased dramatically, which is reflected by both the experimental and predicted results.

Fig. 18 shows the comparison of peak and stabilised forces between experimental and prediction results. The effect of step size on both peak and stabilised forces are predicted accurately and the largest prediction error is 8.25 % with step size of 1 mm. Among different tool radius, with values of 24.82 % and 25.69 %, the largest prediction errors of peak and stabilised forces appear when tool radius is 10 mm. While, with tool radius of 5 mm, the prediction errors are calculated as small as 5.96 % and 3.27 % for peak and stabilised forces, respectively. The effect of drawing angle on peak and stabilised forces is also predicted to have good agreement with experimental ones, with the largest error of 9.15 % for the peak force and 11.45 % for stabilised force. The peak force always rises with the increase of drawing angle, while there is a drop of stabilised force when larger drawing angles are used, which is reflected by the developed model. For different sheet thickness, the worst prediction accuracy of peak force appears at thickness of 0.85 mm with prediction error of 12.55 %, while poor prediction of stabilised force is observed at 2 mm thickness with error of 15.24 %. The above comparison demonstrates that the developed model has the capability to predict both stabilised and peak forces with high accuracy because of the consideration of both local deformation and global bending in ISF.

3.4. Model validation of force components

To validate the new analytical model for different force components, the comparison between prediction and experimental results of the peak vertical (F_{v_p}), stabilised vertical (F_{v_s}) and horizontal forces is shown in Fig. 19. The experimental data come from the study by Aerens et al. (2010). For different step size, the analytical model can predict the force components well, while the worst prediction results are given by the horizontal force, the largest error of which is 19.53 %. As shown in Fig. 19(c) and (d), when the tool radius is 10 mm, some discrepancy in peak and stabilised vertical forces is observed with prediction error of 25.77 % and 27.19 %. However, for smaller tool dimension, the prediction is more accurate. Fig. 19(e) and (f) reveals that the tendency of force components with the increase of drawing angle is predicted accurately, especially the vertical component of peak force. While the prediction error of horizontal force shows large values at small drawing angles because of the low force level and gradually reversed radial force, which is a result of the change in size relationship between Parts A and B. As depicted in Fig. 19(g) and (h), the analytical model exhibits higher accuracy with thinner sheet. ISF of 2 mm sheet shows the largest prediction deviation of peak vertical and horizontal forces, with error of 20.13 % and 24.09 %, respectively. The above analysis indicates that, the analytical model can predict the vertical and horizontal components of both peak and stabilised forces in different ISF conditions.

3.5. Comparison between the new analytical model and other models

Since the validation of the developed analytical model is demonstrated in the above sections, this section aims to compare the new analytical model to some force prediction models with high reputation. As two of the representative studies for force prediction in ISF, Aerens et al. (2010) model is experimental based, while Chang et al. (2019) model were derived on the basis of theoretical analysis in ISF. In Aerens et al. model, the prediction equation of stabilised vertical force is expressed as following (Aerens et al., 2010):

$$F_{v\_s} = 0.0716 \bullet R_m \bullet {t_0}^{1.57} \bullet {d_{tool}}^{0.41} \bullet \Delta h^{0.09} \bullet \alpha \bullet \cos\alpha \quad (66)$$

where R_m is ultimate tensile strength, d_{tool} is tool diameter and Δh is scallop height.

Chang et al. model calculates the forming force as multiplication of the contact area and the through-thickness stress on neutral surface. The total force is decomposed to force components by projecting contact area in different directions on coordinate planes.

Distinctively, the new model is more focused on the deformation behaviour in ISF and decomposes the effect of different force components for separate calculation. The current model also considered the change of deformation condition, geometric feature, indentation effect, elastic recovery and global bending effect, which are neglected in literature but important issues. The only similarity between Chang et al. model and this model is that both put the identification of contact region in an important position. Chang et al. model uses this to calculate the size of contact area, but the new model uses the defined region to calculate the localised shear force.

Adjusted coefficient of determination (R^2_{adj}) and root mean square error (*RMSE*) are used to evaluate and compare the models. Larger R^2_{adj} and smaller *RMSE* indicate more accurate prediction. As shown in Fig. 20, the evaluation and comparison are made based on vertical force results in ISF of AA3003-O by Aerens et al. (2010).

For different step size, the prediction results of the new model have better agreement with experimental results than Aerens et al. and Chang et al. models when the step size is smaller than 0.75 mm, but shows worse accuracy with step size of 1 mm. The R^2_{adj} value of the new model is 0.1827, which is smaller than Chang et al. model, and this may be a

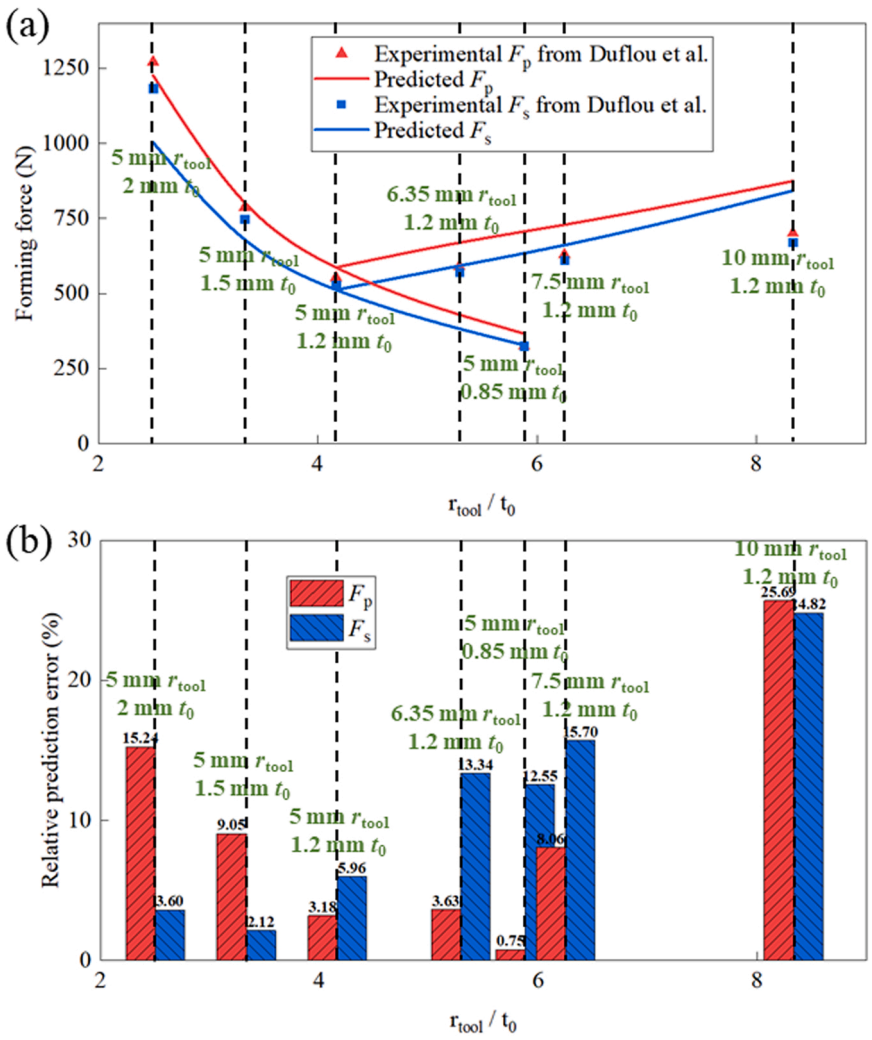

Fig. 22. Effect of the ratio r_{tool}/t_0 on (a) comparison between predicted peak force F_p and stabilised force F_s and experimental results from Duflou et al. (2007a). The specific tool radius and sheet thickness for different r_{tool}/t_0 values are marked in (a) and (b).

result that the prediction results by the new model are always smaller than experimental results. However, the smallest *RMSE* of 27.88 N indicates the good prediction effect of the new model. For different tool dimensions, the best prediction is provided by the new model at tool radius smaller than 7.5 mm. At a tool radius of 10 mm, the predicted force by the new model shows the largest deviation, which also leads to the largest *RMSE*. As presented in Fig. 20(e), more accurate prediction is given by the new model at medium and high drawing angles, especially from 40° to 60°. The medium R^2_{adj} and *RMSE* of the new model in Fig. 20 (f) indicate that the new model can give better prediction than Chang et al. model but is less accurate than Aerens et al. model for different drawing angles. For different sheet thickness, the best prediction is made by Aerens et al. model, while the new model could achieve the best prediction accuracy for ISF of thin sheet with thickness of 0.85 mm and 1.2 mm. It is noteworthy that in some cases the R^2_{adj} values of the compared models are 0, and this may be caused by that the prediction is always larger or smaller than experiment. It could be concluded that in the current study the new model makes better prediction than Aerens et al. and Chang et al. models, especially in common ISF conditions.

4. Discussions

As shown in Sections 2.5 and 2.6, the frictional coefficient between forming tool and sheet material has an influence on the forming force in ISF, while the model validation in Sections 3.3 and 3.4 indicates that the tool dimension and sheet thickness have more effect on the prediction accuracy than other process parameters. This section discusses possible improvement with the consideration of lubrication condition on the forming force and the effect of tool-sheet dimensional interaction on the prediction accuracy.

4.1. Effect of lubrication condition

As there are only lubricant types but no definite frictional coefficient given in previous publications, only a sensitivity analysis on the effect of frictional coefficient is discussed without detailed validation in this section. The analytically predicted force history, stabilised total force, and force components with different frictional coefficient can be found in Fig. 21. Other process conditions of the studied cases are the same as the base test as given in Section 3.3.

As shown in Fig. 21, the frictional coefficient does not have any influence on the vertical force but has an obvious influence on the horizontal force. This is also indicated by the analytical modelling process. As the horizontal force is much smaller than the vertical force, the total force is less influenced by frictional coefficient, i.e., lubrication condition. In the analytical results, a wide range of frictional coefficients are applied, only slight change of the total force is observed. This is consistent with the testing result from Duflou et al. (2007a), in which, with the use of lubricants, the peak force varied between 350 N and

365 N and the stabilised force was about 320 N in all cases. It is only in the case with no lubricant used that the peak force reached 375 N. Therefore, the lubrication condition may have a notable influence on the horizontal force and the accurate identification of frictional coefficient between forming tool and sheet material in ISF plays an important role in the prediction of horizontal force, which may be beneficial to the improvement of the analytical model.

4.2. Effect of the tool-sheet interaction on prediction accuracy

As investigated by Silva et al. (2011), the interaction between sheet thickness and tool radius has an influence on material formability, deformation, and fracture behaviour. This section assesses the tool-sheet interaction and its effect on the forming force prediction accuracy.

In Section 3, the prediction accuracy of the new analytical model is reduced with the increase of the tool radius and the sheet thickness. When the sheet is relatively thin compared to the tool dimension, the local deformation may be close to the behaviour in stretch forming, where stretching, bending and through-thickness shearing dominate the material deformation. The indentation effect becomes more obvious when the sheet thickness is larger in ISF. This makes a slight change of deformation behaviour in ISF, which is essential to the analytical derivation of the model. Therefore, the ratio between the tool radius and the sheet thickness r_{tool}/t_0 should be considered as an important parameter in ISF. Fig. 22 gives the effect of ratio r_{tool}/t_0 on the comparison between the analytical results and experimental stabilised force F_s and peak force F_p from Duflou et al. (2007a) in ISF of AA3003-O. With ratio r_{tool}/t_0 from 4.16 to 5.88, there are two prediction values for a certain r_{tool}/t_0. This is because for the same ratio r_{tool}/t_0, the tool radius and sheet thickness are different and lead to different predicted forces. As shown in Fig. 22, for ISF of AA3003-O, the most favourable prediction of the stabilised force F_s and the peak force F_p is given when the ratio r_{tool}/t_0 reaches 3.3 and 5.88, respectively, for ISF of AA3003-O. In the conditions of smaller or larger ratio r_{tool}/t_0, less accurate prediction is observed, which reflects that the new model does not have enough flexibility to capture the change of local deformation behaviour due to the tool-sheet dimensional relationship. Therefore, further improvement is needed to make the analytical model more robust in more extensive range of tool dimension and sheet thickness.

5. Conclusions

This work provides a novel analytical method to predict the forming force history in ISF. A number of less investigated but important issues are considered in the modelling, which gives more insight and mechanics explanation of the complicated and instable forming process. The main conclusions of this work can be drawn as follows:

(1) A novel force prediction model is developed and implemented for ISF with analytical method by revealing the deformation mechanism and localised tool-sheet contact. The validity is confirmed by a series of ISF tests with different shapes, materials, and process parameters. The developed model is also validated by effective prediction of the forming force history in ISF processing of TA1 cranial plate.
(2) Sudden changes in deformation state, contact condition, thickness distribution under contact, local material deformation and global bending are cooperatively considered in the analytical model. The factors are proven to be essential in predicting forming force history and force components in ISF. This work also presents the first attempt for the peak force prediction, which is well modelled and validated.
(3) The analytical model enables detailed prediction of forming force components and gives a direct correlation to different material deformation modes. The experimental data and prediction results show distinctive characterisations of both the vertical and horizontal forces in forming different geometries under plane strain and biaxial tension conditions.
(4) Compared with the models developed by Aerens et al. and Chang et al., the new model in this study shows advantages in predicting both peak and stabilised forces. It can reflect the remarkable fluctuation of forming forces in ISF of truncated pyramid parts and hence give more accurate prediction in most ISF cases.
(5) The selection of frictional coefficient and the interaction between tool dimension and sheet thickness may affect the prediction results. The prediction accuracy can be further improved by more precise measurement of frictional coefficient and more precise reflection of deformation behaviour with the change of tool-sheet dimensional relationship.

CRediT authorship contribution statement

Hui Zhu: Conceptualization, Methodology, Investigation, Data curation, Software, Formal analysis, Validation, Visualization, Writing – original draft. **Hengan Ou:** Conceptualization, Methodology, Validation, Writing – review & editing, Supervision, Funding acquisition.

Declaration of Competing Interest

The authors declare that they have no known competing financial interests or personal relationships that could have appeared to influence the work reported in this paper.

Data Availability

Data can be made available with institution's approval.

Acknowledgements

The first author would like to acknowledge the financial support of Faculty of Engineering Research Excellence PhD Scholarship awarded by the University of Nottingham. This work was supported by the Engineering and Physical Sciences Research Council [Grant no. EP/W010089/1].

Appendix A. Derivation of thickness distribution in the whole contact region in 3D space

To derive the thickness distribution of the whole contact region, the 3D coordinate system should be used. As mentioned in Section 2.1 and illustrated in Fig. 2, for a proposed position on the top surface of the sheet, the spherical coordinates are $(r_{tool}, \varphi, \theta)$.

If the selected position is in ND region, it must be in Part A. Through this position, the thickness along the circumferential direction would vary from t_0 at the position of $(r_{tool}, \beta, \theta)$ as shown in Fig. A1(a), to the thickness at the projection position on the workpiece meridional cross-section, the coordinates of which are supposed as $(r_{tool}, \varphi_p, \pi)$. The relationship between φ and φ_p can be expressed as following:

$$\varphi_p = -\arcsin(\sin\varphi \bullet \cos\theta) \tag{A1}$$

The thickness of the projection position $(r_{tool}, \varphi_p, \pi)$ can be obtained as below:

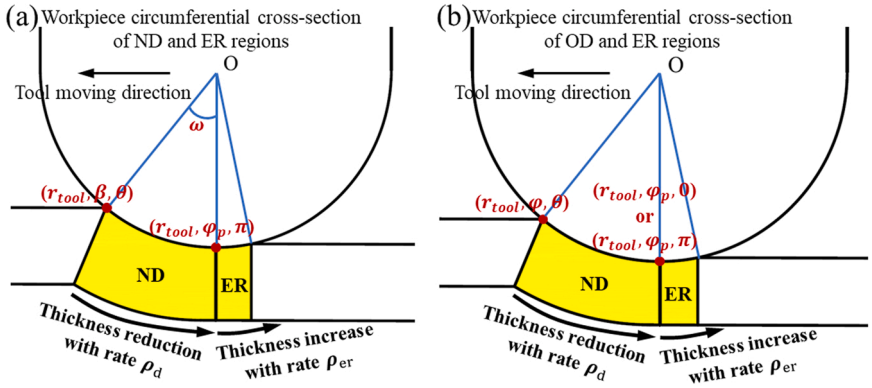

Fig. A1. Illustration of thickness distribution in the workpiece circumferential cross-section of (a) ND, ER regions and (b) OD, ER regions.

$$t_p = t_0 - \frac{t_0 \bullet (1-\cos\alpha) \bullet [\beta + \arcsin(\sin\varphi \bullet \cos\theta)]}{\alpha + \beta} \tag{A2}$$

According to the assumption, the thickness from $(r_{tool}, \beta, \theta)$ to $(r_{tool}, \varphi_p, \pi)$ is linearly distributed along a circular arc, and the arc angle (ω) can be approximately expressed as following:

$$\omega = \frac{\sqrt{(r_{tool} \bullet \beta)^2 - (r_{tool} \bullet \beta_1)^2}}{\sqrt{r_{tool}^2 - (r_{tool} \bullet \sin\beta_1)^2}} = \frac{\sqrt{\beta^2 - \beta_1^2}}{\sqrt{1 - (\sin\beta_1)^2}} \tag{A3}$$

The thickness reduction rate ρ_d of ND region along workpiece circumferential direction may be calculated as following:

$$\rho_d = \frac{t_0 - \left[t_0 - \frac{t_0 \bullet (1-\cos\alpha) \bullet (\beta - \beta_1)}{\alpha + \beta}\right]}{\frac{\sqrt{\beta^2 - \beta_1^2}}{\sqrt{1-(\sin\beta_1)^2}}} = \frac{t_0 \bullet (1-\cos\alpha) \bullet (\beta - \beta_1) \bullet \sqrt{1 - (\sin\beta_1)^2}}{(\alpha + \beta) \bullet \sqrt{\beta^2 - \beta_1^2}} \tag{A4}$$

As a result, the thickness at position $(r_{tool}, \varphi, \theta)$ in ND region can be written as the expression below:

$$t = t_p + \rho_d \bullet \frac{r_{tool} \bullet \varphi \bullet \sin\theta}{\sqrt{r_{tool}^2 - (r_{tool} \bullet \sin\varphi \bullet \cos\theta)^2}} \tag{A5}$$

And Eq. (13) in Section 2.2 can be obtained for the thickness distribution in ND region.

In OD region as shown in Fig. A1(b), the thickness increases from the projection position on the workpiece meridional cross-section along the circumferential direction with the same increase rate ρ_d. In Part A, the relationship between φ and φ_p is given as Eq. (A1), while in Part B, it can be calculated as following:

$$\varphi_p = \arcsin(\sin\varphi \bullet \cos\theta) \tag{A6}$$

Subsequently, no matter in Part A or B, the thickness of the projection position can be expressed as Eq. (A2) uniformly, and the thickness at position $(r_{tool}, \varphi, \theta)$ in OD region is derived the same to Eq. (13) in ND region.

In ER region, as the thickness increase Δt_{er} at the maximum elastic recovery position is given in Eq. (5), combining the thickness expression t_c under the tool centre position in Eq. (9), the increase rate ρ_{er} along the circular arc in Fig. A1(a) and (b) can be calculated using the following equation:

$$\rho_{er} = \frac{\left[\exp\left(\frac{1}{2} \bullet \frac{\bar{\sigma}_c}{E}\right) - 1\right] \bullet \frac{t_0 \bullet (1-\cos\alpha) \bullet \beta}{\alpha + \beta}}{\arccos\left\{1 - \left[\exp\left(\frac{1}{2} \bullet \frac{\bar{\sigma}_c}{E}\right) - 1\right] \bullet \frac{t_0 \bullet (1-\cos\alpha) \bullet \beta}{r_{tool} \bullet (\alpha + \beta)}\right\}} \tag{A7}$$

For the proposed position $(r_{tool}, \varphi, \theta)$, the φ_p coordinate of the projection position is derived as Eq. (A1) in Part A or Eq. (A6) in Part B of ER region. The thickness of the projection position is derived as Eq. (A2), the same as the ones in ND and OD regions. Therefore, in the workpiece circumferential direction, the thickness in both Part A and B of ER region can be uniformly expressed as the below equation:

$$t = t_p + \rho_{er} \bullet \frac{-r_{tool} \bullet \varphi \bullet \sin\theta}{\sqrt{r_{tool}^2 - (r_{tool} \bullet \sin\varphi \bullet \cos\theta)^2}} \tag{A8}$$

Embedding Eqs. (A2) and (A7) in Eq. (A8), it gives the thickness expression in ER region as Eq. (14) in Section 2.2.

References

Aerens, R., Eyckens, P., Van Bael, A., Duflou, J.R., 2010. Force prediction for single point incremental forming deduced from experimental and FEM observations. Int. J. Adv. Manuf. Technol. 46, 969–982.

Ai, S., Lu, B., Chen, J., Long, H., Ou, H., 2017. Evaluation of deformation stability and fracture mechanism in incremental sheet forming. Int. J. Mech. Sci. 124, 174–184.

Allwood, J., Houghton, N., Jackson, K., 2005. The design of an incremental sheet forming machine. Adv. Mater. Res. Trans. Tech. Publ. 6, 471–478.

Ambrogio, G., Filice, L., Micari, F., 2006. A force measuring based strategy for failure prevention in incremental forming. J. Mater. Process. Technol. 177, 413–416.

Bansal, A., Lingam, R., Yadav, S.K., Reddy, N.V., 2017. Prediction of forming forces in single point incremental forming. J. Manuf. Process. 28, 486–493.

Bowen, D.T., Russo, I.M., Cleaver, C.J., Allwood, J.M., Loukaides, E.G., 2022. From art to part: learning from the traditional smith in developing flexible sheet metal forming processes. J. Mater. Process. Technol. 299, 117337.
Cao, T.T., Lu, B., Xu, D.K., Zhang, H., Chen, J., Long, H., Cao, J., 2015. An efficient method for thickness prediction in multi-pass incremental sheet forming. Int. J. Adv. Manuf. Technol. 77, 469–483.
Centeno, G., Silva, M.B., Cristino, V.A.M., Vallellano, C., Martins, P.A.F., 2012. Hole-flanging by incremental sheet forming. Int. J. Mach. Tools Manuf. 59, 46–54.
Chang, Z., Chen, J., 2019. Analytical model and experimental validation of surface roughness for incremental sheet metal forming parts. Int. J. Mach. Tools Manuf. 146, 103453.
Chang, Z., Chen, J., 2022. Investigations on the forming characteristics of a novel flexible incremental sheet forming method for low-ductility metals at room temperature. J. Mater. Process. Technol. 301, 117456.
Chang, Z., Li, M., Chen, J., 2019. Analytical modeling and experimental validation of the forming force in several typical incremental sheet forming processes. Int. J. Mach. Tools Manuf. 140, 62–76.
Cooper, D.R., Gutowski, T.G., 2020. Prospective environmental analyses of emerging technology: a critique, a proposed methodology, and a case study on incremental sheet forming. J. Ind. Ecol. 24, 38–51.
Duflou, J., Tunckol, Y., Szekeres, A., Vanherck, P., 2007a. Experimental study on force measurements for single point incremental forming. J. Mater. Process. Technol. 189, 65–72.
Duflou, J.R., Tunckol, Y., Aerens, R., 2007b. Force analysis for single point incremental forming. Key Eng. Mater. Trans. Tech. Publ. 344, 543–550.
Duflou, J.R., Habraken, A.-M., Cao, J., Malhotra, R., Bambach, M., Adams, D., Vanhove, H., Mohammadi, A., Jeswiet, J., 2017. Single point incremental forming: state-of-the-art and prospects. Int. J. Mater. Form. 11, 743–773.
Emmens, W., Sebastiani, G., van den Boogaard, A.H., 2010. The technology of incremental sheet forming—a brief review of the history. J. Mater. Process. Technol. 210, 981–997.
Fang, Y., Lu, B., Chen, J., Xu, D.K., Ou, H., 2014. Analytical and experimental investigations on deformation mechanism and fracture behavior in single point incremental forming. J. Mater. Process. Technol. 214, 1503–1515.
Filice, L., Ambrogio, G., Micari, F., 2006. On-line control of single point incremental forming operations through punch force monitoring. CIRP Ann.-Manuf. Technol. 55, 245–248.
Hagan, E., Jeswiet, J., 2003. Effect of wall angle on Al 3003 strain hardening for parts formed by computer numerical control incremental forming. Proc. I Mech. Eng. B-J. Eng. 217, 1571–1579.
Hu, J., Marciniak, Z., Duncan, J., 2002. Mechanics of Sheet Metal Forming. Elsevier.
Hussain, G., Gao, L., 2007. A novel method to test the thinning limits of sheet metals in negative incremental forming. Int. J. Mach. Tools Manuf. 47, 419–435.
Jackson, K., Allwood, J., 2009. The mechanics of incremental sheet forming. J. Mater. Process. Technol. 209, 1158–1174.
Jiang, Z., Ehmann, K.F., Cao, J., 2022. Prediction of forming temperature in electrically-assisted double-sided incremental forming using a neural network. J. Mater. Process. Technol. 302, 117486.
Kopac, J., Kampus, Z., 2005. Incremental sheet metal forming on CNC milling machine-tool. J. Mater. Process. Technol. 162, 622–628.
Kumar, A., Gulati, V., Kumar, P., Singh, H., 2019. Forming force in incremental sheet forming: a comparative analysis of the state of the art. J. Braz. Soc. Mech. Sci. Eng. 41, 251.
Li, Y.L., Daniel, W.J.T., Liu, Z.B., Lu, H.B., Meehan, P.A., 2015. Deformation mechanics and efficient force prediction in single point incremental forming. J. Mater. Process. Technol. 221, 100–111.
Liu, F., Li, Y., Yuan, H., Sun, R., Li, F., Li, J., 2022. Comprehensive modeling of forming forces in three directions for incremental sheet forming process based on the contact area. J. Manuf. Process. 84, 986–1000.
Lu, B., Fang, Y., Xu, D.K., Chen, J., Ou, H., Moser, N.H., Cao, J., 2014. Mechanism investigation of friction-related effects in single point incremental forming using a developed oblique roller-ball tool. Int. J. Mach. Tools Manuf. 85, 14–29.
Lu, B., Ou, H., Shi, S.Q., Long, H., Chen, J., 2016. Titanium based cranial reconstruction using incremental sheet forming. Int. J. Mater. Form. 9, 361–370.
Martins, P.A.F., Bay, N., Skjoedt, M., Silva, M.B., 2008. Theory of single point incremental forming. CIRP Ann.-Manuf. Technol. 57, 247–252.
Mohanty, S., Regalla, S.P., Daseswara Rao, Y., 2019. Robot-assisted incremental sheet metal forming under the different forming condition. J. Braz. Soc. Mech. Sci. Eng. 41, 1–12.
Moser, N., Leem, D., Ehmann, K., Cao, J., 2021. A high-fidelity simulation of double-sided incremental forming: improving the accuracy by incorporating the effects of machine compliance. J. Mater. Process. Technol. 295, 117152.
Najm, S.M., Paniti, I., 2023. Investigation and machine learning-based prediction of parametric effects of single point incremental forming on pillow effect and wall profile of AlMn1Mg1 aluminum alloy sheets. J. Intell. Manuf. 34, 331–367.
Nirala, H.K., Agrawal, A., 2022. Adaptive increment based uniform sheet stretching in Incremental Sheet Forming (ISF) for curvilinear profiles. J. Mater. Process. Technol. 306, 117610.
Obikawa, T., Satou, S., Hakutani, T., 2009. Dieless incremental micro-forming of miniature shell objects of aluminum foils. Int. J. Mach. Tools Manuf. 49, 906–915.
Ostasevicius, V., Paleviciute, I., Paulauskaite-Taraseviciene, A., Jurenas, V., Eidukynas, D., Kizauskiene, L., 2021. Comparative analysis of machine learning methods for predicting robotized incremental metal sheet forming force. Sensors 22, 18.
Park, J.J., Kim, Y.H., 2003. Fundamental studies on the incremental sheet metal forming technique. J. Mater. Process. Technol. 140, 447–453.
Praveen, K., Lingam, R., Reddy, N.V., 2020. Tool path design system to enhance accuracy during double sided incremental forming: an analytical model to predict compensations for small/large components. J. Manuf. Process. 58, 510–523.
Ren, H., Li, F., Moser, N., Leem, D., Li, T., Ehmann, K., Cao, J., 2018. General contact force control algorithm in double-sided incremental forming. CIRP Ann. 67, 381–384.
Schafer, T., Schraft, R.D., 2005. Incremental sheet metal forming by industrial robots. Rapid Prototyp. J. 11, 278–286.
Silva, M.B., Skjoedt, M., Martins, P.A.F., Bay, N., 2008. Revisiting the fundamentals of single point incremental forming by means of membrane analysis. Int. J. Mach. Tools Manuf. 48, 73–83.
Silva, M.B., Nielsen, P.S., Bay, N., Martins, P.A.F., 2011. Failure mechanisms in single-point incremental forming of metals. Int. J. Adv. Manuf. Technol. 56, 893–903.
Takano, H., Kitazawa, K., Goto, T., 2008. Incremental forming of nonuniform sheet metal: possibility of cold recycling process of sheet metal waste. Int. J. Mach. Tools Manuf. 48, 477–482.
Wu, R., Li, M., Cai, S., Liu, X., Yang, M., Huang, W., Chen, J., 2020. Analytical model for temperature prediction in friction stir–assisted incremental forming with synchronous bonding of dissimilar sheet metals. Int. J. Adv. Manuf. Technol. 107, 2177–2187.
Zhu, H., Ou, H., Popov, A., 2020. Incremental sheet forming of thermoplastics: a review. Int. J. Adv. Manuf. Technol. 111, 565–587.